Optogenetic and chemical genetic tools for rapid repositioning of vimentin intermediate filaments

Milena Pasolli [1]*, Joyce C. M. Meiring [1]*, James P. Conboy [2],

Gijsje H. Koenderink [2] and Anna Akhmanova [1]

[1] Cell Biology, Neurobiology and Biophysics, Department of Biology, Faculty of Science, Utrecht University, Padualaan, Utrecht, 3584 CS, The Netherlands.

[2] Department of Bionanoscience, Kavli Institute of Nanoscience Delft, Delft University of Technology, 2629 HZ Delft, The Netherlands.

* Equal contribution

Corresponding author: Anna Akhmanova, a.akhmanova@uu.nl

Abstract

Intermediate filaments (IFs) are a key component of the cytoskeleton, essential for regulating cell mechanics, maintaining nuclear integrity, positioning organelles, and modulating cell signaling. Unlike actin filaments and microtubules, IFs have slower dynamics, and current insights into IF function primarily come from studies using long-term perturbations, such as protein depletion or mutation. Here, we present tools that allow rapid manipulation of vimentin IFs in the whole cytoplasm or within specific subcellular regions by inducibly coupling them to microtubule motors, either pharmacologically or using light. Perinuclear clustering of vimentin had no strong effect on the actin or microtubule organization, cell spreading, and focal adhesions, but reduced cell stiffness. Mitochondria and endoplasmic reticulum sheets were repositioned together with vimentin, whereas lysosomes were only briefly repositioned and rapidly regained their normal distribution. Keratin was displaced along with vimentin in some cell lines but remained intact in others. Our tools help to study the immediate effects of vimentin perturbation and identify direct links of vimentin to other cellular structures.

Introduction

Intermediate filaments (IFs), along with actin and microtubules, are among the three major cytoskeletal systems in mammalian cells (Herrmann and Aebi, 2004). Unlike microtubules and actin, IFs lack polarity, exhibit much slower dynamics and are extremely resilient and elastic (Etienne-Manneville, 2018; Herrmann et al., 2007). Among them, vimentin, a type III IF protein, is a prominent component of cells of mesenchymal origin (Mendez et al., 2010). Recent structural work indicated that vimentin forms a helical structure of 40 α-helices organized into five protofibrils that are connected by the vimentin tails, with the head domains located in the lumen (Eibauer et al., 2024). Vimentin IFs surround the nucleus and spread throughout the cytoplasm, a distribution facilitated by microtubule-based motors (Hookway et al., 2015; Robert et al., 2019). Additionally, due to interactions with actin filaments, the vimentin network is subject to actin-driven retrograde flow (Leduc and Etienne-Manneville, 2017).

Vimentin plays an important role in many cellular processes, such as cell mechanics and control of cell stiffness (Guo et al., 2013), maintenance of cell shape, cell-substrate adhesion (Bhattacharya et al., 2009) and cell migration (Eckes et al., 1998). Furthermore, vimentin participates in templating and stabilizing microtubule networks (Gan et al., 2016; Schaedel et al., 2021) and is involved in the positioning and anchorage of organelles such as mitochondria (Nekrasova et al., 2011), endo-lysosomes, and endoplasmic reticulum (ER) (Cremer et al., 2023). Finally, vimentin plays a role in signaling and gene regulation (Paulin et al., 2022).

The cellular functions of vimentin have been primarily studied using knockout and knockdown approaches (Bhattacharya et al., 2009; Colucci-Guyon et al., 1994; Eckes et al., 2000; Kural et al., 2007; Mendez et al., 2014; Mohanasundaram et al., 2022; Ostrowska-Podhorodecka et al., 2022). While these studies have provided insights into the consequences of vimentin loss, they could not distinguish the direct and immediate interactions and interdependencies between vimentin and other cellular structures from the long-term effects caused by the absence of vimentin and the ensuing compensatory cellular changes, including alterations in gene expression.

Treatments perturbing vimentin organization have also been used to study its function (Ridge et al., 2016). For example, overexpression of defective gigaxonin, an E3 ligase adaptor, induces dense perinuclear aggregation of vimentin filaments (Bomont, 2016; Mahammad et al., 2013). Similarly, withaferin A, a natural product with anti-tumor and anti-angiogenesis properties, reorganizes vimentin into perinuclear aggregates but lacks specificity, impacting not only other IFs but also actin and microtubules (Bargagna-Mohan et al., 2007; Grin et al., 2012). Another pharmacological agent, simvastatin, was shown to induce bundling and collapse of vimentin filaments (Lavenus et al., 2020; Trogden et al., 2018), but its use as a tool is complicated by additional effects, such as its impact on cholesterol synthesis. Furthermore, microinjected mimetic peptides were used to disrupt filament assembly and rapidly reorganize the vimentin network (Goldman et al., 1996; Helfand et al., 2011). While these

peptides act quickly—causing changes within minutes—they often disrupt other cytoskeletal components, leading to cellular alterations like rounding and blebbing (Goldman et al., 1996). Their specificity is further limited as they are derived from conserved IF regions (Strelkov et al., 2002), potentially affecting other IF networks. Additionally, microinjection requires specialized expertise and equipment, reducing accessibility and reproducibility. Altogether, this underlines the need for more precise tools to reorganize vimentin IFs and directly observe their interactions and effects on other cellular structures.

In this study, we developed a robust method to rapidly relocalize vimentin filaments, either locally or globally, by recruiting to them microtubule-based motors using either chemical or light-induced heterodimerization. This allowed us to observe vimentin interactions and interdependencies with other cellular structures and their dynamic behavior on a time scale of 15-60 minutes, which is too short to alter gene expression. We found that clustering of vimentin in the cell center by microtubule minus-end-directed kinesins had only mild effects on the actin and microtubule cytoskeleton, and no major impact on cell spreading and focal adhesions, but strongly reduced cell stiffness. The keratin-8 network was not affected by vimentin displacement in HeLa cells but was co-clustered with vimentin in U2OS and COS-7 cell lines, supporting the cell-type-specific nature of IF organization. ER sheets and mitochondria were relocalized together with vimentin, confirming their direct interactions. In contrast, lysosomes were only mildly affected, and their normal distribution was rapidly restored. Our method enables acute and controlled studies of the role of vimentin in cytoskeletal crosstalk and organelle positioning and dynamics, revealing short-term effects and steady-state alterations.

Results

Chemically induced repositioning of vimentin to microtubule plus or minus ends

To induce rapid repositioning of vimentin IFs, we used a chemically inducible heterodimerization system to recruit to vimentin microtubule-based motors, as described previously for membrane organelles (Kapitein et al., 2010). This system takes advantage of the polarized organization of microtubules, which in dividing cells have their minus ends predominantly anchored in the cell center whereas the plus ends radiate outward. In such cells, recruitment of minus-end-directed motors concentrates cargoes near the cell nucleus, whereas plus-end-directed motors disperse cargoes towards the cell periphery (Kapitein et al., 2010).

The system we used was based on inducible binding of two protein domains, FRB and FKBP, upon the addition of a rapamycin analog (rapalog AP21967, also known as A/C heterodimerizer) (Clackson et al., 1998; Pollock et al., 2000). We fused the FKBP domain and a fluorescent marker, mCherry, to the C-terminus of vimentin (Figure 1A, B), as this is the preferred tagging site for avoiding aggregation and ensuring proper filament assembly (Herrmann et al., 1996; Usman et al., 2022). The FRB domain was fused to a kinesin motor to induce controlled movement. To trigger minus-end-directed transport, we employed the motor domain (amino acids 861–1321) of a moss kinesin-14 type VI kinesin-14b from the moss *Physcomitrella patens* (hereafter referred to as ppKin14)(Jonsson et al., 2015). The motor was tetramerized through a fusion with the leucine zipper domain of GCN4 (Nijenhuis et al., 2020), and tagged with a BFP fluorescent marker for visualization (Chen et al., 2022). This motor protein was selected because by itself, it does not perturb endogenous transport in mammalian cells but can efficiently pull cargoes when artificially coupled to them (Nijenhuis et al., 2020). For plus-end-directed transport, we used a hemagglutinin (HA)-tagged dimeric motor domain fragment of the neuronal kinesin-1 KIF5A (amino acids 1–560) (Figure 1A, B). This motor was chosen for its demonstrated efficiency in pulling the highly interconnected and abundant ER network, which spans the entire cell (Özkan et al., 2021). Given its properties, we anticipated that KIF5A would similarly perform effectively in pulling the vimentin filament network. Flexible glycine-serine (GS) linkers were inserted between the fusion protein domains to ensure proper protein folding and functionality.

We hypothesized that the vimentin-mCherry-FKBP (Vim-mCh-FKBP) fusion would incorporate into vimentin IFs, and in the presence of rapalog, would recruit the FRB tagged kinesins and drive redistribution of the whole vimentin network. Heterodimerization with ppKin14 was expected to relocate vimentin towards the microtubule-organizing center (MTOC), whereas heterodimerization with KIF5A was expected to move it to microtubule plus ends at the cell periphery (Figure 1C). This hypothesis was initially tested in COS-7 cells, which were transiently transfected with the fusion constructs, fixed after one hour of treatment with ethanol solvent with or without rapalog and stained for total vimentin, or in the case of the plus-end-directed motor, for the HA tag (Figure 1D-E). The mCherry-tagged vimentin strongly

colocalized with total vimentin (Figure 1 D-E, Figure S1A), and the signal and the distribution of the latter appeared largely unperturbed in the absence of rapalog, though the fraction of the cell area occupied by vimentin was slightly larger in transfected cells than in untransfected control cells (Figure 1F). To assess the efficacy of the tool, we analyzed cells with comparable expression levels of the constructs treated with either rapalog or solvent control (Figure 1F-I). Treatment with rapalog for 1 hour had no effect on vimentin distribution in untransfected cells; however, in transfected cells the vimentin network was completely collapsed (Figure 1D-F). In ppKin14 transfected cells, a single vimentin cluster was formed at the cell center, as expected. Surprisingly, the outcome in cells expressing KIF5A was quite similar, with a major vimentin cluster in the cell center and some additional, smaller clusters in the peripheral cytoplasm (Figure 1E, F). Similar results were obtained in U2OS cells (Figure S1B-C), indicating that these effects were not cell line-specific.

To observe vimentin relocalization in real time, we performed live cell imaging before and after rapalog addition (Figure 1J, L). We observed that vimentin repositioning towards microtubule minus ends with ppKin14 occurred rapidly, with strong vimentin clustering observed already within 10 min, likely due to the dense nature of the vimentin network in the cell center (Figure 1J, Video S1). The effect of KIF5A was slower (clustering visible within 20 min) and resulted in a pronounced tug-of-war (Video S2 and S3), leading to the formation of vimentin clusters at microtubule crossroads at the cell periphery in addition to vimentin accumulation in the cell center, where its initial density was the highest (Figure 1L). After an hour of rapalog treatment, cells were fixed and stained for total vimentin, confirming its repositioning (Figure 1K, M). Taken together, our findings demonstrate that the rapalog-induced kinesin recruitment can trigger rapid vimentin displacement from most of the cytoplasm, with the minus-end-directed ppKin14 organizing a single centrally positioned cluster, and the plus-end-directed KIF5A forming additional smaller clusters at the cell periphery.

Light-induced vimentin repositioning

We next modified the system by substituting the FKBP and FRB domains for the components of the improved Light Induced Dimerizer (iLID) system (Guntas et al., 2015). This system consists of an optimized LOV2 domain derived from *Avena sativa* conjugated to the bacterial peptide SsrA (iLID), and the SsrA-interacting domain SspB. In the dark state, the SsrA in iLID is sterically blocked by LOV2, but upon LOV2 activation with blue light, SsrA becomes available for binding by SspB (Guntas et al., 2015). We fused the iLID to the two kinesin motors and linked the mCherry-tagged C-terminus of vimentin to $SspB_{micro}$ (Figure 2A, B). Illumination with blue light was expected to cause motor recruitment and relocalization of vimentin, similar to the FRB-FKPB system (Figure 2B, C). This was indeed observed in U2OS cells transiently transfected with iLID-GFP-GCN4-ppKin14 and Vim-mCh-SspB after 45 minutes of whole cell blue light illumination, and subsequent fixation and cell staining for total vimentin (Figure 2D, E). To assess the performance of the tool, we analyzed cells with comparable

expression levels, evaluated by fluorescence intensity of the tags of the transfected constructs (Figure 2F, G). Within the optimized expression range, clustering of vimentin in the cell center was observed only in transfected cells, and only upon blue light illumination (Figure 2D, E). This treatment had no effect on the cell area, indicating that vimentin clustering had no major effect on cell spreading (Figure 2H).

The advantage of light-induced heterodimerization is that it can also be used for subcellular manipulations. Indeed, by using local illumination with blue light, we could cause vimentin retraction in a part of the cell, without affecting vimentin distribution in the rest of the cytoplasm (Figure 2I, J). Subsequent fixation and staining for vimentin confirmed that endogenous vimentin was also locally displaced along with the tagged vimentin (Figure 2K).

Another advantage of the iLID-SspB system compared to the rapalog-induced heterodimerization is that it is reversible. In order to evaluate reversibility, we first exposed transfected U2OS cells to 30 minutes of intermittent blue light, which resulted in vimentin clustering in the center of the cell, and then continued imaging the tagged vimentin without blue light to allow cells to recover (Figure 2L, Video S4). Cells required between 2.5 and 4 hours to restore vimentin distribution (Figure 2L, M), likely through a combination of diffusion and active transport by the kinesin-1 motor, which transports vimentin filaments toward the cell periphery (Robert et al., 2019). While some cells exhibited complete recovery, others regained only 40-70% of the initial vimentin density at the periphery. This variability may be attributed to differences in construct expression levels and the high degree of vimentin compaction near the MTOC, potentially including crosslinking proteins trapped within the dense mesh (Figure 2M)(Petitjean et al., 2024; Wiche and Winter, 2011).

Finally, we also tested optogenetic vimentin repositioning in combination with the KIF5A-iLID fusion by whole cell illumination and found that it worked similarly to KIF5A-FRB: vimentin formed some peripheral clusters, with a significant part of the filaments accumulating in the cell center (Figure S2A-C). Repositioning vimentin with a minus-end-directed kinesin proved more effective than with a plus-end-directed motor, likely due to the dense organization of the vimentin network in the perinuclear region.

Clustering of vimentin has little effect on microtubules, actin, and focal adhesions

Considering that microtubules and vimentin can reciprocally affect each other (Gan et al., 2016; Prahlad et al., 1998; Schaedel et al., 2021), we next investigated whether vimentin clustering affects microtubule organization. To this end, COS-7 cells were co-transfected with Vim-mCh-FKBP and either FRB-BFP-GCN4-ppKin14 or HA-KIF5A-FRB, with non-transfected cells serving as controls (Figure 3A, B). After one hour treatment with or without rapalog, the cells were fixed and stained for tyrosinated tubulin, a marker of dynamic microtubules. The overall microtubule intensity did not differ between transfected and non-transfected cells, nor between rapalog-treated and untreated conditions (Figure 3C). However, we noted that the microtubule network appeared slightly more disorganized in transfected cells, likely due

to the overexpression of vimentin and motor proteins. This disorganization was not significantly different after pulling vimentin in either direction, as quantified by the ratio of non-radial to radial microtubules (Figure 3D).

Next, we examined whether stable microtubules would be affected by vimentin pulling. Given that COS-7 cells displayed variable levels of stable microtubules, as indicated by acetylated tubulin staining (data not shown), we performed these experiments in U2OS cells, which have much more consistent levels of stable microtubules. Cells were fixed after one hour of treatment with or without rapalog. Cells co-expressing Vim-mCh-FKBP and FRB-BFP-GCN4-ppKin14 exhibited similar levels of acetylated tubulin intensity compared to non-transfected cells, regardless of the treatment condition (Figure 3E, G). However, cells co-expressing Vim-mCh-FKBP with HA-KIF5A-FRB showed significantly reduced acetylated tubulin levels even without rapalog addition (Figure 3E, G). This is consistent with a recent study showing that overexpression of kinesin-1 KIF5B fragment 1-560 reduces the number of stable, acetylated microtubules (Andreu-Carbó et al., 2024), which are the preferred tracks for this motor in cells (Cai et al., 2009; Dunn et al., 2008; Reed et al., 2006). Due to this strong effect of the KIF5A motor on stable microtubules, we decided to focus on minus-end-directed pulling in subsequent experiments to avoid any indirect effects of perturbing stable microtubules on the studied structures.

We next examined the effects of vimentin clustering on actin stress fibers and focal adhesions, structures that have been reported to be linked to vimentin IFs (Bhattacharya et al., 2009; Esue et al., 2006; Jiu et al., 2015; Mendez et al., 2010). One hour after initiating rapalog-induced vimentin network relocalization by ppKin14, COS-7 cells were fixed and stained for total vimentin, F-actin, and the focal adhesion marker paxillin. Despite strong vimentin clustering, we observed no changes in the cell area, the appearance of F-actin structures, or the number of focal adhesions (Figure 4A-C). We repeated these experiments in U2OS cells, which have more prominent stress fibers and focal adhesions, but again observed no significant changes after vimentin repositioning (Figure 4D-F). This is consistent with the results of light-induced vimentin repositioning described above, where no effect on cell area was observed (Figure 2H). Our findings indicate that the clearance of vimentin from the cytoplasm and its clustering in the cell center do not have significant short-term effects on microtubules, actin, or the ability of cells to spread.

Co-dependency of keratin-8 and vimentin localization is cell-type dependent

We next examined the impact of rapalog-inducible vimentin clustering on keratin IFs using COS-7, U2OS, and HeLa cells. All three cell lines showed endogenous expression of keratin-8, with the highest expression observed in HeLa cells (Figure 5A, Figure S3). In COS-7 cells, vimentin exhibited strong colocalization with the keratin-8 network, which persisted after vimentin clustering (Figure 5B, C). Similarly, U2OS cells showed high vimentin-keratin-8 colocalization, although keratin-8 appeared somewhat more abundant than vimentin at the cell periphery (Figure 5D, E). Vimentin pulling efficiently cleared keratin-8 from the cytoplasm

(Figure 5D, E). This indicates a strong interdependence between the two IF types in COS-7 and U2OS cells.

In HeLa cells, both networks are dense around the nucleus, but the keratin-8 network displays a broader distribution, extending throughout the cell and forming connections to the plasma membrane via desmosomes (Figure 5F) (Jones and Goldman, 1985; Nishizawa et al., 2005; Schwarz et al., 2015). Unlike in COS-7 and U2OS cells, the vimentin and keratin-8 networks in HeLa cells were more distinct, with a lower colocalization coefficient (Figure 5G). Vimentin clustering did not affect the distribution of keratin-8, as reflected by a significant reduction in colocalization (Figure 5F, G). These results suggest a fundamental difference in the interaction of vimentin and keratin-8 networks between cell types. While COS-7 and U2OS cells display a high degree of interdependence, in HeLa cells the two IF networks appear to lack physical connectivity.

Vimentin relocalization to the MTOC reduces cell stiffness

Previous studies have demonstrated that cells lacking vimentin exhibit reduced stiffness and increased deformability (Mendez et al., 2014; Messica et al., 2017; Shaebani et al., 2022). Building on these findings, we aimed to investigate the effect of vimentin reorganization on cellular mechanical properties, with a particular focus on cell stiffness. To explore this, we used rapalog induced vimentin reorganization in U2OS cells (Figure 6A) and measured cell stiffness using a spherical nanoindenter to determine the Young's modulus (Figure S4). Indentations were performed at three locations within the perinuclear region (Figure 6B). Cells in which vimentin was pulled toward the cell center exhibited a reduction in Young's modulus of more than 60% compared to control cells (Figure 6C). This significant decrease in cell stiffness indicates that vimentin reorganization makes U2OS cells softer and more deformable, aligning with previous findings from vimentin knockout studies (Mendez et al., 2014; Messica et al., 2017; Shaebani et al., 2022).

Vimentin pulling drives ER reorganization and reveals redundancy of ER-vimentin linkers

Next, we investigated the effect of vimentin repositioning on intracellular membranes. Vimentin and the ER display a significant degree of co-localization, especially in the perinuclear area where ER sheets are present, as well as at the more peripherally located ER matrices (Cremer et al., 2023; Lynch et al., 2013; Nixon-Abell et al., 2016) (Figure 7A, B). At the cell periphery, ER intensity decreases, coinciding with the polygonal ER network and a sparser vimentin distribution (Figure 7A, B).

Using the optogenetic tool, we observed that ER sheets and matrices were pulled along with vimentin, confirming their previously described direct connections (Cremer et al., 2023) (black arrows, Figure 7C; Video S5). Most of the vimentin and ER repositioning occurred within approximately 10 minutes (Figure 7C, Video S5). While initially this resulted in a sparser tubular ER network at the cell periphery, over time, the tubular network became denser, with smaller polygonal structures. A similar pattern was seen in fixed COS-7 cells using the rapalog-

based tool to reorganize vimentin (Figure 7D). After one hour of rapalog-induced vimentin clustering, we observed two distinct phenotypes: in some cells, the ER remained sparse and mostly confined to the perinuclear area; in other cells, ER reorganized, forming smaller polygons that extended toward the periphery (Figure 7D).

Next, we investigated the effect of vimentin pulling in the absence of RNF26, a recently described linker between ER sheets and vimentin (Cremer et al., 2023). We used U2OS wild type (WT) and RNF26 knockout cells and performed localized light-induced vimentin relocalization inside a region of interest at the cell periphery (blue dashed box, Figure 8A, B, Video S6 and S7). Surprisingly, even in the absence of RNF26, vimentin pulling still resulted in concomitant retraction of the ER sheets and matrices (Figure 8B; Video S7). This was also demonstrated by the reduction in fluorescence intensity of the ER marker inside the region of interest accompanying the drop in vimentin intensity (Figure 8C). This implies the existence of additional linkers between the ER network and the vimentin cytoskeleton.

Vimentin-mediated mitochondrial re-localization persists after pulling, whereas lysosomes rapidly recover

We next investigated the effects of vimentin repositioning on other organelles. U2OS cells were used, because in these cells, organelles are distributed throughout the cell, whereas in COS-7 cells most organelles are strongly clustered in the perinuclear region, and their relocalization with vimentin would be less obvious. Local vimentin pulling revealed that the clearance of vimentin led to a strong redistribution of mitochondria (Figure 9A, Video S8). Mitochondria remained co-clustered with vimentin also during longer (one hour) treatment periods, as observed in fixed cells after using the rapalog tool (Figure 9B). The fraction of mitochondria at the cell periphery (defined as the cell area outside the perinuclear region, which was empirically defined as a circle with a radius of 13.82 µm) was reduced in rapalog-treated transfected cells compared to untreated transfected cells (Figure 9C).

In contrast, lysosomes demonstrated a different behavior. In optogenetic experiments, lysosomes were initially pulled along with vimentin, but quickly dissociated from the vimentin cluster and returned to the cell periphery (Figure 9D, Video S9). This was confirmed by the long-term (one hour) rapalog treatment and analysis of fixed cells, which showed no significant changes in lysosome distribution between treated and untreated cells (Figure 9E). The lysosome fraction at the cell periphery (outside the perinuclear region) remained the same, ~40% (Figure 9F). These data indicate that vimentin IFs are not a dominant factor in the steady-state distribution of lysosomes.

Discussion

Previous studies investigating the function of vimentin and its interactions with other organelles have commonly employed vimentin mutations, deletions, mimetic peptides or non-specific drugs (Mohan and Bargagna-Mohan, 2016; Nekrasova et al., 2011; Ridge et al., 2016; Saldanha et al., 2023). However, these approaches often disrupt other cytoskeletal systems, alter gene expression, or influence signaling pathways, complicating efforts to determine direct contributions of vimentin to cellular organization (Grin et al., 2012; Ostrowska-Podhorodecka et al., 2022; Paulin et al., 2022; Ridge et al., 2022; Saldanha et al., 2023).

In contrast, our study introduces a rapid chemical and optogenetic approach to reposition the vimentin network, which can be precisely controlled in time and space. In cells with a radial microtubule organization and significant perinuclear clustering of vimentin, as used in this study, minus-end-directed kinesin could rapidly (within ~10 min) clear the cytoplasm of the majority of vimentin filaments, without strongly perturbing either microtubules or the actin cytoskeleton. The optogenetic approach for clustering vimentin was reversible, suggesting that pulling did not damage vimentin filaments. The recovery was, however, incomplete in some cells, potentially due to variability in construct expression or because the forces generated by kinesin-1 (Robert et al., 2019) may be insufficient to fully restore vimentin's original distribution. Vimentin clustering might cause increased crosslinking via their tail domains (Aufderhorst-Roberts and Koenderink, 2019; Lin et al., 2010), or perhaps by proteins like plectin becoming trapped within the filament mesh (Foisner et al., 1988; Wiche and Baker, 1982; Wiche and Winter, 2011). Future studies could improve the robustness of reversible assays by better controlling expression levels of the fusion constructs, for example by generating stable cell lines with inducible protein expression.

Our findings confirmed established functions of the vimentin network and provided new insights into its interactions with other cellular structures. Unlike previous approaches to perturb vimentin that often affected the organization of other cytoskeletal components such as microtubules, actin stress fibers and focal adhesions (De Pascalis et al., 2018; Grin et al., 2012; Havel et al., 2014; Saldanha et al., 2023; Swoger et al., 2022), our chemical and optogenetic manipulation of vimentin did not have a marked effect on these structures. This suggests that the changes in the actin or microtubule networks resulting from vimentin perturbation might occur over longer time frames or may depend on changes in signaling or gene expression induced by vimentin loss. Furthermore, cell type may also play a significant role. For example, rapidly migrating cells, characterized by faster adhesion turnover rates (Gupton and Waterman-Storer, 2006; Mavrakis and Juanes, 2023) and larger focal adhesions (Kim and Wirtz, 2013) may react differently to vimentin perturbation. Finally, since previous work has suggested that cells migrating on soft substrates are more sensitive to the loss of vimentin (Swoger et al., 2022), it would be interesting to test whether the same phenotypes can be reproduced with inducible vimentin clustering.

We identified cell-type-specific differences in the interactions between vimentin and keratin. In COS-7 and U2OS cells, which express both keratin-8 and vimentin (Sha et al., 2019), vimentin appears to play a dominant role. In these cells, keratin-8 IFs were pulled along with vimentin. However, in HeLa cells, vimentin clustering did not impact the keratin network, raising intriguing questions about the physical connections between IFs across different cell types. Vimentin relocalization led to a drastic reduction in stiffness of U2OS cells, consistent with findings from vimentin knockout cells (Mendez et al., 2014; Messica et al., 2017; Shaebani et al., 2022). Since we did not observe any changes in the actin or microtubule cytoskeleton in the time frame of the experiment but did find that keratin-8 co-clusters with vimentin in analyzed cells, we conclude that IFs by themselves make a major contribution to cell rigidity.

We also examined the relationship between vimentin and the endoplasmic reticulum (ER), building on previous findings (Cremer et al., 2023; Lynch et al., 2013). Colocalization of the vimentin and ER networks, particularly ER matrices (Nixon-Abell et al., 2016) and sheets during acute vimentin displacement confirmed their physical interaction. Notably, even in the absence of vimentin-ER linker, RNF26, ER displacement together with vimentin was still observed, implying the existence of other linkers. This suggests potential redundancy in ER-vimentin linkages and demonstrates the utility of our vimentin pulling tool for exploring molecular connections.

In addition to the ER, other organelles were affected by vimentin pulling. Mitochondria moved together and remained co-clustered with vimentin, consistent with previous observations that vimentin influences mitochondrial positioning (Nekrasova et al., 2011). Meanwhile, lysosomes showed only transient interactions with vimentin, as a fraction of lysosomes co-clustered with vimentin during pulling but rapidly regained their distribution after vimentin clustering. This suggests a much weaker interaction, probably mediated by the contacts with the ER network (Kilpatrick et al., 2013; Özkan et al., 2021).

In summary, our vimentin-pulling tool is versatile and can be applied across various cell types and systems. Future optimizations, such as tagging and pulling endogenous vimentin using a knock-in approach or generation of clonal stable cell lines, could help minimize side effects associated with vimentin and motor protein overexpression, and improve the reproducibility of reversible pulling assays. This tool holds significant potential for advancing our understanding of vimentin's role in cellular organization, including both its direct and indirect effects. It could shed light on cytoskeletal dependencies, cell protrusion and migration, and distinguish the immediate effects of vimentin reorganization on cell architecture from the long-term impact on signaling pathways and gene expression.

Materials & Methods

Chemicals, peptides, and recombinant proteins	Company	Catalog number
SiR-tubulin	Spirochrome	SC014
Janelia Fluor 646 HaloTag Ligand	Promega	GA1120
FuGENE 6	Promega	E2692
Pen/strep	Gibco	15140-122
Gibson Assembly Master Mix	Thermo Fisher	A46629
ProLong™ Glass Antifade Mountant	Thermo Fisher Scientific/Life Tech	P36984
16% PFA Methanol-free	Fisher Emergo	28908
Aqueous Glutaraldehyde EM Grade, 10%	Electron Microscopy Sciences	16110
A/C Heterodimerizer (rapalog)	Takara	AP21967
A/C Heterodimerizer (rapalog)	Bio Connect	635056

Cell lines		
HeLa Kyoto	Narumiya S., Kyoto University	CVCL_1922
COS-7	ATCC	CVCL_0224
U2OS	ATCC	CVCL_0042
U2OS RNF26 KO	Berlin I., Leiden University Medical Center (Cremer et al., 2023)	

Recombinant DNA	
FRB-BFP-GCN4-ppKin14	Chen et al. 2022
HA-KIF5A-FRB	This paper
Vim-mCh-FKBP	This paper
iLID-GFP-GCN4-ppKin14	This paper
KIF5A-mVenus-iLID	This paper
Vim-mCh-SspB	This paper
Halo-KDEL	Meiring et al. 2022
Halo-mitoTag	This paper
LAMP1-Halo	Meiring et al. 2022

Software-plugins

FIJI	ImageJ	https://imagej.net/software/fiji/downloads
ComDet plugin	Fiji	https://github.com/ekatrukha/ComDet
Radiality map plugin	Fiji	https://github.com/UU-cellbiology/radialitymap
Radius plugin	Fiji	https://gist.github.com/ekatrukha/105553627f1bee01367faae153bfe5c0

MtrackJ	Smal et al. (2008)	N/A
Sigma Plot	Systat Software Inc.	7
Excel	Microsoft	Office16
Prism	Graphpad	10.1.1(323)
MetaMorph	Molecular Devices	7.10.2.240
Dataviewer	Optics11	2

Cell culture and transfections

COS-7, HeLa, U2OS wild-type, and RNF26 knockout cells were cultured in Dulbecco's Modified Eagle Medium (DMEM; Sigma), supplemented with 10% fetal calf serum (FCS), 100 U/ml penicillin, and 100 µg/ml streptomycin (1% Pen Strep; Sigma). Cells were maintained at 37 °C in a humidified atmosphere with 5% CO2 and were regularly tested for mycoplasma contamination. For immunostaining, cells were plated on 18 mm coverslips, while 25 mm coverslips or gridded dishes (Lonza) were used for live cell imaging. Gridded dishes were used if cells needed to be first imaged live and then found back after fixing and staining. Transient transfections were performed using the Fugene 6 transfection reagent, following the manufacturer's protocol. For optogenetic construct transfections in 6 well plates, 2 µg Vim-mCh-SspB and 500 ng iLID-GFP-GCN4-ppKin14 or 200 ng KIF5A-mVenus-iLID was used per well; for 12 well plates the quantity was halved. For chemical pulling experiments in 6-well plates, each well was transfected with 500 ng of Vim-mCh-FKBP and either 250 ng of FRB-BFP-GCN4-ppKin14 or HA-KIF5A-FRB. In 12-well plates, the quantities were also halved. Cells were subjected to rapalog treatments, live cell imaging, or fixation one day post-transfection.

Drug treatment

For rapalog-inducible dimerization experiments, cells were plated on 18 mm cover glasses and co-transfected the following day with Vim-mCh-FKBP and either FRB-BFP-GCN4-ppKin14 or HA-KIF5A-FRB constructs. Twenty-four hours post-transfection, cells were treated with 400 nM rapalog (AP21967 A/C heterodimerizer, Takara) for one hour.

Plasmids and cloning

The Vim-mCh-FKBP construct was generated using PCR-based cloning combined with Gibson assembly. The mCherry-N1 construct served as the backbone, with vimentin amplified from human cDNA encoding isoform 1 of vimentin (corresponding to CCDS7120, 466 amino acids), and the FKBP domain amplified from the FKBP-mCherry-CAMSAP2 plasmid (Chen et al., 2022). GS linkers were included between protein segments. The FRB-BFP-GCN4-ppKin14 was described previously (Chen et al., 2022). In order to make Vim-mCh-SspB, Vimentin was first amplified from from human cDNA encoding isoform 1 (VIM-201, protein 466aa) and cloned in to the KIF1A(1-365)-GFP-SspB plasmid (Addgene #174629) (Nijenhuis et al., 2020) replacing

KIF1A, cut out using AscI and XbaI restriction sites, by Gibson assembly, next the GFP was replaced by the mCherry from SspB-mCh-p60 (Addgene #190168) (Meiring et al., 2022) by restriction enzyme cloning using XbaI and NheI restriction sites. The iLID-GFP-GCN4-ppKin14 was generated from SspB-GFP-GCN4-ppKin14 (Addgene #174640)(Nijenhuis et al., 2020) by restriction enzyme cloning using AscI and XbaI restriction sites to replace the SspB with the iLID from iLID-mCl3-Tau0N4R (Meiring et al., 2022). The KIF5A-mVenus-iLID was cloned by first substituting the SspB in KIF1A(1-365)-Venus-SspB (Addgene #174635) (Nijenhuis et al., 2020) for an iLID from EB3N-VVDfast-mCl3-iLID (Addgene #190165) (Meiring et al., 2022) by restriction enzyme cloning using NheI and NdeI restriction sides, and subsequently replacing the KIF1A with KIF5A amplified from 3xHA-KIF5A-FRB using AscI and XbaI restriction sites and Gibson assembly. The Halo-Mitotag was made by cutting out the Rab6a from Halo-Rab6a (Addgene #190171) (Meiring et al., 2022) using KpnI and BamHI and inserting the C-terminal tail of the actA protein as a mitochondrial targeting sequence (Zhu et al., 1996) 5'-TTAATTCTTGCAATGTTAGCTATTGGCGTGTTCTCTTTAGGGGCGTTTATCAAAATTATTCAATTAAGAAA AAATAAT -3' by Gibson assembly. Halo-KDEL and LAMP1-Halo were previously described in (Meiring et al., 2022). 3xHA-KIF5A-FRB was kindly provided by Ginny Farías (Utrecht University, The Netherlands). mCherry-N1, KIF1A-GFP-SspB, KIF1A(1-365)-mVenus-SspB, (1-365)-GFP-SspB and SspB-GFP-GCN4-ppKin14 were gifts from Lukas Kapitein (Utrecht University, The Netherlands). All constructs were confirmed by DNA sequencing.

Antibodies, immunofluorescence staining, and Western blotting

Different fixation methods were employed depending on the target protein for immunofluorescence experiments. For vimentin, microtubules, and keratin-8, cells were fixed on ice in ice-cold methanol for 15 minutes. For calnexin staining, cells were fixed with 0.1% glutaraldehyde (GA), 4% paraformaldehyde (PFA), and 4% sucrose pre-warmed at 37°C for 10 minutes at room temperature. Cytochrome C, Lamtor4, phalloidin, and paxillin staining were performed on cells fixed in 4% PFA in PBS for 10 minutes at room temperature. Post-fixation, cells were washed thrice with PBS and, unless methanol fixed, permeabilized with 0.2% Triton X-100 in PBS for 2.5 minutes. Following another washing step with PBS, cells fixed with GA were quenched with 100 mM sodium borohydride in PBS three times, 5 minutes each. After another PBS washing step, cells were blocked in 2% BSA in PBS for an hour at room temperature. The incubation of the primary and secondary antibodies was done at room temperature for an hour, with the antibodies diluted in 2% BSA in PBS. Phalloidin conjugated to 647 fluorophore was added with the secondary antibodies. Between the primary and secondary antibody incubations, there was a washing step with 0.05% Tween-20 in PBS. After the last wash, coverslips were mounted with ProLong Gold mounting media.

The following primary antibodies were used in this study:

Primary antibodies Antibody	**Host**	**Company**	**Catalog number**	**Dilution** IF /WB
Actin c4	Mouse	Sigma-Aldrich/Merck	MAB1501	-/1:1000

Calnexin	Rabbit	Abcam	22595	1:250
Cytochrome C	Mouse	BD Pharmingen	556432	1:200
Cytokeratin-8 (K8/KRT8)	Rat	DSHB, TROMA-I	AB_531826	1:12/ 1:100
HA	Rat	Covance		1:200
LAMTOR4 (D6A4V)	Rabbit	Cell Signalling	12284	1:200
Paxillin	Mouse	BD Biosciences	610619	1:200
Tubulin-acetylated	Mouse	Sigma-Aldrich	T7451-200UL	1:200
Tubulin-alpha YL1/2 (tyrosinated)	Rat	Pierce/Thermo	MA1-80017	1:400
Vimentin	Chicken	Abcam	ab24525	1:200
Vimentin	Rabbit	Abcam	ab92547	1:400
Vimentin V9	Mouse	Sigma-Aldrich	V6630	1:200/ 1:1000

Alexa Fluor −405,–488, –594 and −647 conjugated highly cross-preabsorbed goat antibodies against rabbit, rat, and mouse IgG were used as secondary antibodies. Anti-rabbit and anti-rat secondary antibodies were from Thermo Fischer, anti-mouse secondary antibodies were from Jackson ImmunoResearch. Secondary antibodies were all used at a dilution of 1:200/250.

For Western blotting, cells were harvested at 90–100% confluency from a 10 cm dish. Lysis was performed using RIPA buffer, supplemented with protease and phosphatase inhibitors (Roche). Proteins were separated on 10% polyacrylamide gels and transferred onto 0.45 µm nitrocellulose membranes (Sigma-Aldrich). Membrane blocking was performed in 2% BSA in PBS for 30 minutes at room temperature. The membrane was initially exposed to primary antibodies overnight at 4°C, then washed three times with 0.05% Tween-20 in PBS. Next, IRDye 680LT and 800CW anti-mouse and anti-rat secondary antibodies (LI-COR Biosciences) diluted 1:1,000 in 2% BSA in PBS were added, and the membrane was incubated for one hour at room temperature before being washed again with 0.05% Tween-20 in PBS. Finally, membranes were imaged on an Odyssey CLx infrared imaging system (Image Studio version 5.2.5, LI-COR Biosciences).

HaloTag labelling

HaloTag dye JF646 (Promega) was diluted in DMSO to 200 µM, aliquoted and stored at -20 °C. Aliquoted HaloTag dye was diluted 1:10,000 in prewarmed cell media, vortexed for 5 s and incubated with cells overnight.

Microscopy

Leica SP8 confocal microscopy

We conducted confocal or gated STED imaging using a Leica TCS SP8 STED 3 X microscope, controlled by LAS X software. The setup included an HC PL APO 100x/1.4 oil STED WHITE objective, with white laser excitation at 488, 577, and 633 nm and depletion at 775 nm using a pulsed laser. Images were captured in 2D STED mode with a vortex phase mask. The Leica

PMT and HyD hybrid detector were used, with a time gate range of 0.5 to 9 ns, and depletion laser power was set at 50%. Images were primarily acquired using confocal microscopy; instances where STED mode was used are explicitly noted in the figure legends.

Airyscan confocal microscopy

A Carl Zeiss LSM880 Fast AiryScan microscope equipped with 405 nm, Argon Multiline, 561 nm, and 633 nm lasers as well as AiryScan and PMT detectors was utilized for fixed confocal imaging. Samples were imaged using an Alpha Plan-APO 100x/1.46 Oil DIC VIS objective, and the microscope was operated by ZEN 2.3 software. Images acquired using Airyscan mode are indicated in the figure legends.

Spinning disc microscopy

The Nikon Eclipse Ti-E inverted research microscope was used for spinning disk confocal microscopy. It included a Nikon Perfect Focus System, a Nikon Plan Apo VC 100x N.A. 1.40 oil objective, and a spinning disk confocal scanner unit (CSU-X1-A1, Yokogawa). The system featured a Photometrics PRIME BSI back-illuminated sCMOS camera, an ASI motorized stage with piezo plate MS-2000-XYZ, and MetaMorph 7.10 software. It was equipped with three lasers: a 488 nm, 150 mW Vortran Stradus 488; a 561 nm, 100 mW Coherent OBIS 561-100LS; and a 639 nm, 150 mW Vortran Stradus 639. For imaging, we used the ET-GFP filter set (49002, Chroma) for GFP-tagged proteins, the ET-mCherry filter set (49008, Chroma) for mCherry-tagged proteins, and the ET-Cy5 filter set (49006, Chroma) for HaloTag JF646-tagged proteins. To maintain the cells at 37°C we used a stage incubator (STXG-PLAMX-SETZ21L, Tokai Hit). For localized illumination experiments the iLas FRAP system controlled with iLas software (Gataca Systems) was used.

Optogenetic vimentin pulling

For whole cell illumination fixed experiments cells were either protected from light and fixed in a dark room with only red and green light (DARK) OR placed on a blue LED array and illuminated for 45 minutes (800 $\mu W/cm^2$) (LIT). Live cell imaging experiments were performed on a spinning disc microscope, using a 488 nm laser to activate iLID-SspB. For whole cell activation either one 500 ms exposure (0.25 mW, 300 $\mu W/cm^2$) every 4 s or one 1 s exposure (0.25 mW, 300 $\mu W/cm^2$) every 30 s was used. For localized activation a FRAP unit was used to apply one localized scan with a duration of 113 ms (3 µW, 700 $\mu W/cm^2$) every 4 s.

Cell stiffness measurements

U2OS cells were seeded in 35 mm glass-bottom dishes (World Precision Instruments) and allowed to adhere overnight. Cells were subsequently transfected as described above, and stiffness measurements were performed the following day. The Young's modulus of cells before and after vimentin pulling was measured using a Chiaro Nanoindenter (Optics11 Life). We indented cells with a spherical tip with 3.5 µm radius, attached to a flexible cantilever with a stiffness of 0.027 N/m. Indentations were made with a loading rate of 2 µm/s to a

depth of 1.5 µm. For vimentin-pulled cells, we waited 30 minutes after adding rapalog before performing indentation measurements. The Chiaro Nanoindenter was mounted on a THUNDER epifluorescence microscope (Leica), allowing us to identify transfected cells. Cells selected for indentation were successfully co-transfected with Vim-mCh-FKBP and FRB-BFP-GCN4-ppKin14Young's modulus was calculated from measured force-distance curves using the Hertzian contact model by the Optics11 Life Dataviewer software (version 2). Each cell was indented at three separate locations in the perinuclear region. Measurements without a distinct contact point or with an otherwise unreliable model fit (<0.9 R^2) were regarded as outliers and excluded from the analysis.

Quantification and statistical analysis

FIJI software was utilized to adjust contrast levels and perform background corrections for image and video preparation. Fluorescence intensity quantification was also carried out in FIJI, with subsequent data processing and normalization completed in Excel. Statistical analysis and graph generation were performed using GraphPad Prism 10.1.1 (323). The Mann-Whitney test was applied for comparisons between two conditions, whereas the Kruskal-Wallis test, followed by Dunn's multiple comparisons test, was used for comparing more than two conditions.

Analysis of fluorescence intensities of transfected constructs

Vim-mCh-SspB, Vim-mCh-FKBP, FRB-BFP-GCN4-ppKin14, iLID-GFP-GCN4-ppKin14, KIF5A-mVenus-iLID, HA-KIF5A-FRB (stained with anti-HA antibody) fluorescence intensities were quantified by defining regions of interest (ROI) around individual cells, including transfected and non-transfected neighboring cells, and a background region for normalization. The mean gray value was measured for each ROI using the following equation:

$$Normalized\ intensity = \frac{(transfected\ cell\ intensity - background)}{(untransfected\ neighbour\ intensity - background)}$$

Quantification of the fraction cell area occupied by vimentin

To quantify the area occupied by vimentin, we thresholded the total vimentin intensity (as obtained by immunofluorescence staining) using the Li threshold algorithm in Fiji and then quantified the total vimentin area using the "Detect Particles" function. This value was then divided by total cell area to calculate cell area occupied by vimentin.

Quantification of vimentin recovery at the cell periphery

Vimentin at cell periphery was analyzed by drawing a ROI near the cell edge, at the cell edge furthest from the MTOC / vimentin cluster, between 10-15 µm in width where the width was perpendicular to the cell edge. ROI was adjusted during cell movement, mean grey value was measured over time inside ROI. Background was subtracted from the measurement and then normalized to the first time point.

Quantification of focal adhesion number

We utilized the ComDet plugin for Fiji (https://github.com/ekatrukha/ComDet) to detect the total number of focal adhesions based on paxillin staining. Phalloidin staining was employed to help define the total cell area. The total number of focal adhesions was then normalized by dividing it by the cell area.

Analysis of microtubule intensity and radiality

To quantify the intensity of tyrosinated tubulin, we used ROIs around transfected and non-transfected cells and background areas. The mean grey value for each ROI was measured and used in the following formula:

$$Normalized\ intensity = \frac{(transfected\ cell\ intensity - background)}{(untransfected\ neighbour\ intensity - background)}$$

To quantify the total intensity of the radial and non-radial microtubules we used the radiality map plugin (https://github.com/UU-cellbiology/radialitymap). After defining radial and non-radial microtubules, we calculated the ratio by dividing the mean intensity of non-radial microtubules by the mean intensity of radial microtubules over the same cell area.

For the quantification of acetylated tubulin, the mean gray values observed after background subtraction were normalized to the average acetylated tubulin intensity in non-transfected cells.

Analysis of vimentin and keratin co-localization

Manders colocalization coefficients for keratin-8 and vimentin networks were calculated using the JACoP plugin in Fiji (Bolte and Cordelières, 2006). Before measuring colocalization, we manually thresholded the images to accurately define the keratin-8 and vimentin networks. Coefficients were calculated from regions of interest (ROIs) with dimensions of 50.2 × 50.2 µm for COS-7 cells, 45.11 × 45.11 µm for U2OS cells, and 35.03 × 35.03 µm for HeLa cells, corresponding to their average cell size. Kruskal–Wallis test with Dunn's multiple comparisons test was used to compare the colocalization coefficients of keratin-8 to vimentin for the different conditions.

Analysis of ER and tagged vimentin intensity during localized vimentin pulling

Localized opto-vimentin pulling experiment in cells co-transfected with Halo-KDEL was analyzed by quantifying mean grey value of Vim-mCh-SspB and Halo-KDEL inside blue light (488 nm) illuminated region over time. Background was subtracted and values were normalized to the first time point.

Analysis of lysosome and mitochondria distribution

Distributions of mitochondria and lysosomes was analyzed using LAMTOR4 and Cytochrome C staining, respectively. The ComDet plugin was used to detect particles, with the cell center

defined at the microtubule organizing center (MTOC). A radius macro was used to calculate the distance of each particle from the cell (https://gist.github.com/ekatrukha/105553627f1bee01367faae153bfe5c0).

From these distance measurements, we determined the fraction of particles located in the cell periphery. The peripheral region was defined as an area beyond a circle with 13.81 µm radius from the MTOC, based on the average size of the perinuclear cloud for U2OS cells. Particles outside this circle were classified as being in the peripheral area of the cell.

Author contributions

M.P. and J.C.M.M. designed and performed experiments, analyzed data and wrote the paper, J.P.C. and G.H.K. performed and analyzed cell stiffness measurements and wrote the paper, A.A. coordinated the project and wrote the paper.

Acknowledgements

We thank L. Kapitein and G. G. Farías (Utrecht University) for providing materials, I. Berlin (Leiden University Medical Center) for sharing RNF26 knockout U2OS cells, and Eugene Katrukha (Utrecht University) for technical support and guidance on image analysis. This work was supported by the Netherlands Organization for Scientific Research (NWO) project ECHO 711018004, EMBO long-term fellowship ALTF 261-2019, OCENW.M20.054, Gravitation programme IMAGINE! (project number 24.005.009), the European Research Council Synergy grant PushingCell (project number 101071793) to A.A. and a grant of NWO Talent Programme (project number VI.C.182.004) to G.H.K.

Competing interests

The authors declare no competing interests.

Figure Legends

Figure 1. Repositioning of the vimentin network by rapalog-induced recruitment of kinesin motors.

(A) A scheme of rapalog-induced heterodimerization constructs. A truncated motor domain of *Physcomitrella patens* kinesin-14b (ppKin14, amino acids 861–1321) is fused to the FRB domain, along with a GCN4 leucine zipper for tetramerization and a BFP tag for detection. A fragment of human KIF5A (amino acids 1–560) is fused to an HA-tagged dimeric motor domain and the FRB domain. The FKBP domain and mCherry were fused to the C-terminus of vimentin. Flexible GS linkers separate protein domains.

(B,C) Schemes illustrating vimentin repositioning triggered by rapalog-induced recruitment of kinesins at the level of a single microtubule **(B)** and in whole cells **(C)**. Without rapalog, Vim-mCh-FKBP does not interact with either FRB-BFP-GCN4-ppKin14 or HA-KIF5A-FRB. Upon rapalog addition, FRB and FKBP heterodimerize, triggering motor attachment to vimentin filaments and their movement along microtubules. Minus-end-directed kinesins trigger vimentin clustering around the MTOC, whereas plus-end-directed kinesins cause the formation of small peripheral clusters and a large perinuclear one.

(D,E) Representative fluorescence images of COS-7 cells co-transfected with Vim-mCh-FKBP and FRB fusions of the indicated motors, with or without 1 hour rapalog treatment. The top panels show untreated cells, whereas the bottom panels display rapalog-treated cells. Transfected cells are outlined with dashed lines, and non-transfected cells serve as controls. Anti-vimentin and anti-HA antibodies detect total vimentin and HA-KIF5A-FRB, respectively.

(F) Quantifications of the fraction of the cell area occupied by vimentin in untransfected and transfected cells with either minus- or plus-end motor constructs, with and without rapalog treatment.

(G-I) Mean fluorescence intensities of Vim-mCh-FKBP intensity **(G)**, FRB-BFP-GCN4-ppKin14 **(H)** and HA-KIF5A-FRB, detected with anti-HA antibody **(I)** per cell, normalized to untransfected cells.

In **(F-I)**, n = 19–34 cells per condition across 3 independent experiments. Plots indicate mean±SD with individual cell measurements shown as dots. ns, not significant; ****, $p < 0.0001$.

(J-L) Live cell imaging reveals the morphology of the vimentin network immediately before and at 10, 20, and 60 min after rapalog addition. Cells co-transfected with ppKin14 **(J)** or KIF5A constructs **(L)** show vimentin reorganization over time.

(K, M) Total vimentin distribution in cells shown in **(J)** and **(L)**, fixed and stained with antibodies against vimentin 60 minutes after rapalog treatment.

Figure 2. Reversible vimentin repositioning by optogenetic recruitment of kinesin motors to vimentin.

(A) Schematic overview of optogenetic vimentin constructs. The constructs are similar to those shown in Figure 1A, except that FRB is substituted for iLID and FKBP for SSB_{micro}. GFP and mVenus are used as fluorescent markers in ppKin14 and KIF5A constructs, respectively.

(B,C) Schematics illustrating the action of the optogenetic vimentin constructs. **(B)** Upon blue light activation the iLID module changes conformation, uncaging a SsrA peptide, which binds to SspB. By tagging vimentin with SspB and ppKin14 and KIF5A with iLID, vimentin can be inducibly pulled towards microtubule minus or plus ends, respectively. **(C)** Transfection of cells with Vim-mCh-SspB combined with one of the two kinesin constructs and blue light activation results in vimentin pulling to microtubule minus or plus-ends, causing vimentin clustering either at the MTOC (ppKin14) or both cell periphery and MTOC (KIF5A).

(D-H) U2OS cells co-transfected with Vim-mCh-SspB and iLID-GFP-GCN4-ppKin14 were either fixed in a dark room (DARK) or exposed to 45 minutes of blue light (LIT) prior to fixation and staining for vimentin (Total vimentin). **(D)** Representative images, with transfected cells outlined with a dashed line. **(E)** Quantification of the fraction of the cell area occupied by vimentin. **(F)** Mean iLID-GFP-GCN4-ppKin14 fluorescence intensity per cell, normalized to untransfected cells. **(G)** Mean cell Vim-mCh-SspB fluorescence intensity. **(H)** Mean total cell area. **(E-H)** n=23-29 cells per treatment analyzed over 3 experiments; bars show mean ± SD. ns, not significant; ****, $p< 0.0001$.

(I-K) U2OS cells co-transfected with Vim-mCh-SspB and iLID-GFP-GCN4-ppKin14 were locally illuminated with 488 nm light pulses for 40 minutes before fixing and staining for vimentin. **(I)** Scheme of the experiment. **(J)** Stills with the region illuminated with blue light indicated with a blue dashed box. **(K)** Vimentin staining in the cell shown in **(J)** fixed after local illumination.

(L-M) U2OS cells co-transfected with Vim-mCh-SspB and iLID-GFP-GCN4-ppKin14 were exposed to whole cell 488 nm light pulses for 30 min to cluster vimentin, and then 488 nm pulses were stopped to allow cells to recover over 4 hours. **(L)** Representative cell directly before light pulses (-30 min), after 30 minutes of 488 nm light pulsing (0 min) and after 4 hours of recovery without blue light activation (4 h). **(M)** Quantification of Vim-mCh-SspB mean intensity at a ROI at the cell periphery over time; plot shows a line for every individual cell, n = 9 cells analyzed over 3 independent experiments.

Figure 3. Effects of vimentin repositioning on the microtubule cytoskeleton.

(A,B) COS-7 cells were co-transfected with Vim-mCh-FKBP and either FRB-BFP-GCN4-ppKin14 or HA-KIF5A-FRB, with non-transfected cells as controls. Transfected cells are outlined with a dashed line. After one hour of treatment with or without rapalog, cells were fixed for analysis. Representative fluorescent images display the microtubule network, labeled with antibodies

against tyrosinated α-tubulin (Tyr-tubulin). Microtubules are further color-coded to indicate radial (cyan) and non-radial (yellow) orientations.

(C) Quantification of tyrosinated α-tubulin intensity in cells expressing Vim-mCh-FKBP along with either FRB-BFP-GCN4-ppKin14 or HA-KIF5A-FRB, normalized to non-transfected cells, with or without rapalog treatment. n = 21-23 cells analyzed across two independent experiments.

(D) Quantification of the ratio of non-radial to radial tyrosinated microtubules in non-transfected cells and cells expressing Vim-mCh-FKBP with either FRB-BFP-GCN4-ppKin14 or HA-KIF5A-FRB, with or without rapalog treatment. n = 20-22 cells were analyzed across two independent experiments.

(E,F) Representative images of U2OS cells stained for acetylated microtubules (Ac-tubulin), showing either untransfected cells or cells co-expressing Vim-mCh-FKBP with either FRB-BFP-GCN4-ppKin14 **(E)** or HA-KIF5A-FRB **(F)**. Transfected cells are outlined with a dashed line. After one hour of treatment with or without rapalog, cells were fixed for analysis.

(G) Quantification of normalized acetylated microtubule intensity in untransfected U2OS cells and cells co-expressing Vim-mCh-FKBP with either FRB-BFP-GCN4-ppKin14 or HA-KIF5A-FRB, in the presence and absence of rapalog. n = 37-49 cells were analyzed across three independent experiments. Plots indicate mean ± SD with individual cell measurements shown as dots. ns, not significant; $*$, $p < 0.05$; $**$, $p < 0.01$; $***$, $p < 0.001$; $****$, $p < 0.0001$.

Figure 4. Effects of vimentin repositioning on the actin cytoskeleton, cell spreading, and focal adhesions.

COS-7 **(A-C)** or U2OS **(D-F)** cells were co-transfected with Vim-mCh-FKBP and FRB-BFP-GCN4-ppKin14, while non-transfected cells served as controls. Transfected cells are outlined with a dashed line.

(A,D) After one hour of treatment with or without rapalog, the cells were fixed and stained for total vimentin, paxillin, and actin using phalloidin.

(B,E) Quantification of the total cell area based on the phalloidin staining in transfected (T) and untransfected (U) cells, with and without rapalog treatment. Dashed boxes show regions enlarged in the Zoom panels.

(C,F) Quantification of the total focal adhesion number based on paxillin staining, normalized to cell area as determined by phalloidin staining in both transfected and untransfected cells, with or without rapalog treatment. Measurements were collected from n = 28-31 cells in **(B)** and **(C)**, and from n = 27-29 cells in **(E)** and **(F)**, across three independent experiments. The plots display the mean ± SD, with individual cell measurements represented as dots. ns, not significant; $*$, $p < 0.05$; $**$, $p < 0.01$; $***$, $p < 0.001$; $****$, $p < 0.0001$.

Figure 5. Effects of vimentin clustering on the keratin-8 network across cell lines.

(A) Expression levels of vimentin and keratin-8 in COS-7, U2OS, and HeLa cells analyzed by Western blotting.

(B,D,F) Indicated cell lines were co-transfected with Vim-mCh-FKBP and FRB-BFP-GCN4-ppKin14 constructs (outlined), while non-transfected cells served as controls. After one hour of treatment with or without rapalog, the cells were fixed for analysis. Total vimentin and keratin-8 network intensities were measured after staining with anti-vimentin and anti-keratin-8 antibodies, respectively.

(C,E,G) Colocalization analysis in COS-7 **(C)**, U2OS **(E)** and HeLa **(G)** cells. The graphs represent Manders' coefficients of thresholded images, measured from 50.2 × 50.2 µm regions of interest (ROIs) per COS-7 cell **(C),** 45.11 × 45.11 µm ROIs per U2OS cell **(E)** and 35.03 × 35.03 µm ROIs per HeLa cell **(G)**. Data are shown as mean ± SD, with individual cell measurements represented by dots. In panel **(C)**, data were collected from n = 25–29 cells; in panel **(E)**, n = 27–29 cells; and in panel **(G)**, n = 27–34 cells, across three independent experiments. ns, not significant; ∗, $p < 0.05$;∗∗, $p < 0.01$; ∗∗∗∗, $p < 0.0001$.

Figure 6. Effects of vimentin repositioning on cell stiffness.

(A, B) Schematic depiction of a control and a rapalog-treated U2OS cell co-transfected with Vim-mCh-FKBP and FRB-BFP-GCN4-ppKin14, before and during indentation in the perinuclear region using a spherical tip of 3.5 µm radius. Each cell was indented at three separate locations in the perinuclear region.

(C) The graph presents the Young's modulus of cells co-transfected with Vim-mCh-FKBP and FRB-BFP-GCN4-ppKin14 constructs, with and without rapalog treatment. Data were collected from n = 19-22 cells across two independent experiments. A total of 56 measurements were obtained from 19 cells without rapalog, and 63 measurements from 22 cells treated with rapalog. The plots display the mean ± SD, with each dot representing an individual cell measurement. ****, $p < 0.0001$.

Figure 7. Effects of vimentin repositioning on ER morphology.

(A) Representative image of a COS-7 cell stained for endogenous calnexin (ER) and vimentin, and **(B)** intensity profile along the indicated line. Images were collected using STED.

(C) U2OS cell co-transfected with Vim-mCh-SspB, iLID-GFP-GCN4-ppKin14 and Halo-KDEL was first imaged for 5 minutes without 488 nm pulsing (-5 min, 0 min), then imaged for 25 minutes

with whole cell 488 nm pulsing to induce optogenetic vimentin clustering (5 min, 10 min, 25 min). Black dashed box shows the region of the cell enlarged in the zoom panels.

(D) Images of COS-7 cells expressing Vim-mCh-FKBP and FRB-BFP-GCN4-ppKin14. Transfected cells are outlined with dashed lines. After one hour of treatment with or without rapalog, cells were fixed and stained for vimentin and calnexin. The images show the distribution of the ER network, visualized by calnexin staining, in both transfected (T) and untransfected (U) cells, in the presence and absence of rapalog. Dashed boxes show the regions that have been enlarged and shown as masks in the zoom images.

Figure 8. Localized optogenetic vimentin repositioning displaces dense ER matrices independent of RNF26.

(A-C) U2OS wild type (WT) **(A)** and RNF26 knockout (KO) **(B)** cells co-transfected with Vim-mCh-SspB, iLID-GFP-GCN4-ppKin14 and Halo-KDEL were pulsed with 488 nm light inside a region of interest at the cell periphery (blue dashed box) for 20 minutes in order to locally displace vimentin. **(A-B)** Example images shown before blue light pulsing (0 min) and 5, 10 and 20 min after localized blue light application. Black dashed box indicates the region of the cell enlarged in zoom images. **(C)** Mean fluorescence intensity of Vim-mCh-SspB and Halo-KDEL (ER) inside the ROI pulsed with blue light was quantified over time and normalized to the first time point after subtracting background. Graph shows mean ± SD, n = 8-9 cells analyzed per group over 3 independent experiments.

Figure 9. Effects of vimentin clustering on the distribution of mitochondria and lysosomes.

(A,D) U2OS cell, co-transfected with Vim-mCh-SspB, iLID-GFP-GCN4-ppKin14 and Halo-MitoTag to label mitochondria **(A)** or LAMP1-Halo to label lysosomes **(D)**, locally illuminated with 488 nm pulses inside a region of interest (blue dashed box) for 10 min **(A)** or with global illumination for 20 min **(D)**. The cell is shown before application of blue light (0 min) and at the indicated time points after blue light pulsing.

(B,E) Imaging of U2OS cells transfected with Vim-mCh-FKBP and FRB-BFP-GCN4-ppKin14 constructs. After one hour of treatment with or without rapalog, cells were subjected to immunostaining for total vimentin and Cytochrome C to label mitochondria **(B)** or LAMTOR4 to label lysosomes **(E)**. Transfected cells are indicated by a dotted outline. Images were acquired with Airyscan mode.

(C,F) The distribution of mitochondria **(C)** or lysosomes **(F)** relative to the microtubule-organizing center (MTOC). Organelles were detected using the ComDet plugin, and their distance from the MTOC was calculated using a radius plugin. The graph shows the percentage of mitochondria or lysosomes located in the peripheral region, which was defined as an area beyond a 13.81 µm radius from the MTOC, with each dot representing data from an individual

cell. Measurements were collected from n = 20-29 cells in **(C)**, and from n = 20-22 cells in **(F)**, across three independent experiments. The plots display the mean ± SD, with individual cell measurements represented as dots. ns, not significant; $**$, $p < 0.01$.

Legends to Supplementary Figures.

Figure S1. Repositioning of the vimentin network in U2OS cells through rapalog-induced recruitment of kinesin motors.

(A) Fluorescence images of COS-7 cells expressing Vim-mCh-FKBP and ppKin14 constructs. The overexpressed vimentin network is visualized by mCherry fluorescence, while total vimentin intensity is detected via anti-vimentin immunostaining. Images were captured using Airyscan microscopy.

(B) Representative fluorescence images of U2OS cells co-transfected with Vim-mCh-FKBP and FRB-BFP-GCN4-ppKin14, with or without 1 hour rapalog treatment. The top panels show untreated cells, while the bottom panels display rapalog-treated cells. Transfected cells are outlined with dashed lines, and non-transfected cells serve as controls. Total vimentin intensity is detected by anti-vimentin immunofluorescence.

(**C**) Images of U2OS cells co-transfected with Vim-mCh-FKBP and HA-KIF5A-FRB, with and without rapalog. Anti-vimentin and anti-HA antibodies detect vimentin and motor protein intensities, respectively.

Figure S2. Optogenetic vimentin pulling with a plus-end-directed kinesin.

(A-C) Schematic of overview of constructs for optogenetic plus end directed vimentin pulling.

(D) U2OS cells co-transfected with Vim-mCh-SspB and KIF5A-mVenus-iLID show vimentin re-localization to clusters in the cell periphery and at the cell center upon blue light activation. Live cell imaging stills shown before blue light activation (0 min) and 10 and 30 minutes after 488 nm pulsing.

Figure S3. Western blot analysis of keratin-8 and vimentin levels in COS-7, U2OS, and HeLa cells

Complete uncropped blots corresponding to the cropped images presented in Figure 5A.

Figure S4. A force-distance curve for cell stiffness measurements.

An example force curve used to determine the Young's modulus of the cells. The raw data is shown in blue and the Hertz model fit is the red line. Fitting was restricted to the first 1.5 µm of indentation, as shown in the figure.

Legends to Supplemental Videos.

Video S1. Rapalog-induced vimentin repositioning by minus-end-directed kinesin.

COS-7 cell co-expressing Vim-mCh-FKBP and FRB-BFP-GCN4-ppKin14. Imaging was conducted for a total of 70 minutes, rapalog is added at the 10-minute mark. Time is shown in hh:mm:ss.

Video S2. Rapalog-induced vimentin repositioning by plus-end-directed kinesin.

COS-7 cell co-expressing Vim-mCh-FKBP and HA-KIF5A-FRB. Total imaging time: 70 minutes, rapalog is added at the 10-minute mark. Time is shown in hh:mm:ss.

Video S3. Rapalog-induced vimentin repositioning by plus-end-directed kinesin.

COS-7 cell co-expressing Vim-mCh-FKBP and HA-KIF5A-FRB. Movie starts from the moment rapalog is added. Time is shown in hh:mm:ss.

Video S4. Light-induced vimentin repositioning and recovery.

U2OS cell co-expressing Vim-mCh-SspB and iLID-GFP-GCN4-ppKin14 was exposed to 1 s of whole cell blue light illumination every 30 s for a total of 30 minutes; a blue dot is shown in the top right corner during blue light illumination. The cell was subsequently imaged for another 4 hours without blue light activation to allow vimentin distribution to recover. Time is shown in hh:mm.

Video S5. Effect of light-induced vimentin repositioning on ER.

U2OS cell co-transfected with Vim-mCh-SspB, iLD-GFP-GCN4-ppKin14 and Halo-KDEL (ER marker) was first imaged for 5 min without blue light, then imaged for another 25 min with 500 ms of whole cell blue light illumination every 4 s; the period of blue light pulsing is indicated by a blue dot in the top right corner. Time is shown in mm:ss.

Video S6. Effect of local light-induced vimentin repositioning on ER in a control cell.

Wild type U2OS cell co-transfected with Vim-mCh-SspB, iLD-GFP-GCN4-ppKin14 and Halo-KDEL (ER marker) was illuminated inside a region of interest (indicated by blue box) with one 113 ms pulse of blue light every 4 s; period of blue light pulsing is indicated by a blue dot in the top right corner. Time is shown in mm:ss.

Video S7. Effect of local light-induced vimentin repositioning on ER in an RNF26 knockout cell.

RNF26 KO U2OS cell co-transfected with Vim-mCh-SspB, iLD-GFP-GCN4-ppKin14 and Halo-KDEL (ER marker) was illuminated inside a region of interest (indicated by blue box) with one 113 ms pulse of blue light every 4 s; period of blue light pulsing is indicated by a blue dot in the top right corner. Time is shown in mm:ss.

Video S8. Effect of local light-induced vimentin repositioning on mitochondria.

U2OS cell co-transfected with Vim-mCh-SspB (magenta), iLD-GFP-GCN4-ppKin14 and Halo-MitoTag (cyan, mitochondria marker) was illuminated inside a region of interest (indicated by blue box) with one 113 ms pulse of blue light every 4 s; period of blue light pulsing is indicated by a blue dot in the top right corner. Time is shown in mm:ss.

Video S9. Effect of light-induced vimentin repositioning on lysosomes.

U2OS cell co-transfected with Vim-mCh-SspB (cyan), iLD-GFP-GCN4-ppKin14 and LAMP1-Halo (yellow, lysosome marker) was exposed to 500 ms of blue light illumination every 4 s; period of blue light pulsing is indicated by a blue dot in the top right corner. Time is shown in mm:ss.

References

Andreu-Carbó, M., C. Egoldt, M.-C. Velluz, C. Aumeier, M. Andreu-Carbó, C. Egoldt, M.-C. Velluz, and C. Aumeier. 2024. Microtubule damage shapes the acetylation gradient. *Nat Commun*. 15:2029.

Aufderhorst-Roberts, A., and G.H. Koenderink. 2019. Stiffening and inelastic fluidization in vimentin intermediate filament networks. *Soft Matter*. 15:7127-7136.

Bargagna-Mohan, P., A. Hamza, Y. Kim, Y. Ho, N. Mor-Vaknin, N. Wendschlag, J. Liu, R.M. Evans, D.M. Markovitz, C.-G. Zhan, K.B. Kim, and R. Mohan. 2007. The tumor inhibitor and antiangiogenic agent withaferin A targets the intermediate filament protein vimentin. *Chem Biol*. 14:623-634.

Bhattacharya, R., A.M. Gonzalez, P.J. DeBiase, H.E. Trejo, R.D. Goldman, F.W. Flitney, and J.C.R. Jones. 2009. Recruitment of vimentin to the cell surface by β3 integrin and plectin mediates adhesion strength. *J Cell Sci*. 122:1390-1400.

Bolte, S., and F.P. Cordelières. 2006. A guided tour into subcellular colocalization analysis in light microscopy. *J Microsc*. 224:213-232.

Bomont, P. 2016. Degradation of the Intermediate Filament Family by Gigaxonin. *Methods Enzymol*. 569:215-231.

Cai, D., D.P. McEwen, J.R. Martens, E. Meyhofer, and K.J. Verhey. 2009. Single molecule imaging reveals differences in microtubule track selection between Kinesin motors. *PLoS Biol*. 7:e1000216.

Chen, F., J. Wu, M.K. Iwanski, D. Jurriens, A. Sandron, M. Pasolli, G. Puma, J.Z. Kromhout, C. Yang, W. Nijenhuis, L.C. Kapitein, F. Berger, and A. Akhmanova. 2022. Self-assembly of pericentriolar material in interphase cells lacking centrioles. *eLife*. 11:e77892.

Clackson, T., W. Yang, L.W. Rozamus, M. Hatada, J.F. Amara, C.T. Rollins, L.F. Stevenson, S.R. Magari, S.A. Wood, N.L. Courage, X. Lu, F. Cerasoli, Jr., M. Gilman, and D.A. Holt. 1998. Redesigning an FKBP-ligand interface to generate chemical dimerizers with novel specificity. *Proc Natl Acad Sci U S A*. 95:10437-10442.

Colucci-Guyon, E., M.M. Portier, I. Dunia, D. Paulin, S. Pournin, and C. Babinet. 1994. Mice lacking vimentin develop and reproduce without an obvious phenotype. *Cell*. 79:679-694.

Cremer, T., L.M. Voortman, E. Bos, M.L. Jongsma, L.R. Ter Haar, J.J. Akkermans, C.M. Talavera Ormeno, R.H. Wijdeven, J. de Vries, R.Q. Kim, G.M. Janssen, P.A. van Veelen, R.I. Koning, J. Neefjes, and I. Berlin. 2023. RNF26 binds perinuclear vimentin filaments to integrate ER and endolysosomal responses to proteotoxic stress. *EMBO J*. 42:e111252.

De Pascalis, C., C. Pérez-González, S. Seetharaman, B. Boëda, B. Vianay, M. Burute, C. Leduc, N. Borghi, X. Trepat, and S. Etienne-Manneville. 2018. Intermediate filaments control collective migration by restricting traction forces and sustaining cell-cell contacts. *J Cell Biol*. 217:3031-3044.

Dunn, S., E.E. Morrison, T.B. Liverpool, C. Molina-París, R.A. Cross, M.C. Alonso, and M. Peckham. 2008. Differential trafficking of Kif5c on tyrosinated and detyrosinated microtubules in live cells. *J Cell Sci*. 121:1085-1095.

Eckes, B., E. Colucci-Guyon, H. Smola, S. Nodder, C. Babinet, T. Krieg, and P. Martin. 2000. Impaired wound healing in embryonic and adult mice lacking vimentin. *J Cell Sci*. 113:2455-2462.

Eckes, B., D. Dogic, E. Colucci-Guyon, N. Wang, A. Maniotis, D. Ingber, A. Merckling, F. Langa, M. Aumailley, A. Delouvée, V. Koteliansky, C. Babinet, and T. Krieg. 1998. Impaired mechanical stability, migration and contractile capacity in vimentin deficient fibroblasts. *J Cell Sci*. 111:1897-1907.

Eibauer, M., M.S. Weber, R. Kronenberg-Tenga, C.T. Beales, R. Boujemaa-Paterski, Y. Turgay, S. Sivagurunathan, J. Kraxner, S. Koster, R.D. Goldman, and O. Medalia. 2024. Vimentin filaments integrate low-complexity domains in a complex helical structure. *Nat Struct Mol Biol*. 31:939-949.

Esue, O., A.A. Carson, Y. Tseng, and D. Wirtz. 2006. A direct interaction between actin and vimentin filaments mediated by the tail domain of vimentin. *J Biol Chem*. 281:30393-30399.

Etienne-Manneville, S. 2018. Cytoplasmic Intermediate Filaments in Cell Biology. *Annu Rev Cell Dev Biol*. 34:1-28.

Foisner, R., F.E. Leichtfried, H. Herrmann, J.V. Small, D. Lawson, and G. Wiche. 1988. Cytoskeleton-associated plectin: in situ localization, in vitro reconstitution, and binding to immobilized intermediate filament proteins. *J Cell Biol*. 106:723-733.

Gan, Z., L. Ding, C.J. Burckhardt, J. Lowery, A. Zaritsky, K. Sitterley, A. Mota, N. Costigliola, C.G. Starker, D.F. Voytas, J. Tytell, R.D. Goldman, and G. Danuser. 2016. Vimentin Intermediate Filaments Template Microtubule Networks to Enhance Persistence in Cell Polarity and Directed Migration. *Cell Syst*. 3:252-263.

Goldman, R.D., S. Khuon, Y.H. Chou, P. Opal, and P.M. Steinert. 1996. The function of intermediate filaments in cell shape and cytoskeletal integrity. *J Cell Biol*. 134:971-983.

Grin, B., S. Mahammad, T. Wedig, M. Cleland, L. Tsai, H. Herrmann, and R.D. Goldman. 2012. Withaferin a alters intermediate filament organization, cell shape and behavior *PloS One*. 7:e39065.

Guntas, G., R.A. Hallett, S.P. Zimmerman, T. Williams, H. Yumerefendi, J.E. Bear, and B. Kuhlman. 2015. Engineering an improved light-induced dimer (iLID) for controlling the localization and activity of signaling proteins. *Proc Natl Acad Sci U S A*. 112:112-117.

Guo, M., Allen J. Ehrlicher, S. Mahammad, H. Fabich, Mikkel H. Jensen, Jeffrey R. Moore, Jeffrey J. Fredberg, Robert D. Goldman, and David A. Weitz. 2013. The role of vimentin intermediate filaments in cortical and cytoplasmic mechanics. *Biophys J*. 105:1562-1568.

Gupton, S.L., and C.M. Waterman-Storer. 2006. Spatiotemporal feedback between actomyosin and focal-adhesion systems optimizes rapid cell migration. *Cell*. 125:1361-1374.

Havel, L.S., E.R. Kline, A.M. Salgueiro, and A.I. Marcus. 2014. Vimentin regulates lung cancer cell adhesion through a VAV2-Rac1 pathway to control focal adhesion kinase activity. *Oncogene*. 34:1979-1990.

Helfand, B.T., M.G. Mendez, S.N. Murthy, D.K. Shumaker, B. Grin, S. Mahammad, U. Aebi, T. Wedig, Y.I. Wu, K.M. Hahn, M. Inagaki, H. Herrmann, and R.D. Goldman. 2011. Vimentin organization modulates the formation of lamellipodia. *Mol Biol Cell*. 22:1274-1289.

Herrmann, H., and U. Aebi. 2004. Intermediate filaments: molecular structure, assembly mechanism, and integration into functionally distinct intracellular scaffolds. *Annu Rev Biochem*. 73:749-789.

Herrmann, H., H. Bär, L. Kreplak, S.V. Strelkov, and U. Aebi. 2007. Intermediate filaments: from cell architecture to nanomechanics. *Nat Rev Mol Cell Biol*. 8:562-573.

Herrmann, H., M. Haner, M. Brettel, S.A. Muller, K.N. Goldie, B. Fedtke, A. Lustig, W.W. Franke, and U. Aebi. 1996. Structure and assembly properties of the intermediate filament protein vimentin: the role of its head, rod and tail domains. *J Mol Biol*. 264:933-953.

Hookway, C., L. Ding, M.W. Davidson, J.Z. Rappoport, G. Danuser, and V.I. Gelfand. 2015. Microtubule-dependent transport and dynamics of vimentin intermediate filaments. *Mol Biol Cell*. 26:1675-1686.

Jiu, Y., J. Lehtimäki, S. Tojkander, F. Cheng, H. Jäälinoja, X. Liu, M. Varjosalo, J.E. Eriksson, and P. Lappalainen. 2015. Bidirectional Interplay between Vimentin Intermediate Filaments and Contractile Actin Stress Fibers. *Cell Rep*. 11:1511-1518.

Jones, J.C., and R.D. Goldman. 1985. Intermediate filaments and the initiation of desmosome assembly. *J Cell Biol*. 101:506-517.

Jonsson, E., M. Yamada, R.D. Vale, and G. Goshima. 2015. Clustering of a kinesin-14 motor enables processive retrograde microtubule-based transport in plants. *Nat Plants*. 1:15087.

Kapitein, L.C., M.A. Schlager, W.A. van der Zwan, P.S. Wulf, N. Keijzer, and C.C. Hoogenraad. 2010. Probing intracellular motor protein activity using an inducible cargo trafficking assay. *Biophys J*. 99:2143-2152.

Kilpatrick, B.S., E.R. Eden, A.H. Schapira, C.E. Futter, and S. Patel. 2013. Direct mobilisation of lysosomal Ca2+ triggers complex Ca2+ signals. *J Cell Sci*. 126:60-66.

Kim, D.-H., and D. Wirtz. 2013. Focal adhesion size uniquely predicts cell migration. *FASEB J*. 27:1351-1361.

Kural, C., A.S. Serpinskaya, Y.H. Chou, R.D. Goldman, V.I. Gelfand, and P.R. Selvin. 2007. Tracking melanosomes inside a cell to study molecular motors and their interaction. *Proc Natl Acad Sci U S A*. 104:5378-5382.

Lavenus, S.B., S.M. Tudor, M.F. Ullo, K.W. Vosatka, and J.S. Logue. 2020. A flexible network of vimentin intermediate filaments promotes migration of amoeboid cancer cells through confined environments. *J Biol Chem*. 295:6700-6709.

Leduc, C., and S. Etienne-Manneville. 2017. Regulation of microtubule-associated motors drives intermediate filament network polarization. *J Cell Biol*. 216:1689-1703.

Lin, Y.C., C.P. Broedersz, A.C. Rowat, T. Wedig, H. Herrmann, F.C. Mackintosh, and D.A. Weitz. 2010. Divalent cations crosslink vimentin intermediate filament tail domains to regulate network mechanics. *J Mol Biol*. 399:637-644.

Lynch, C.D., A.M. Lazar, T. Iskratsch, X. Zhang, and M.P. Sheetz. 2013. Endoplasmic spreading requires coalescence of vimentin intermediate filaments at force-bearing adhesions. *Mol Biol Cell*. 24:21-30.

Mahammad, S., S.N. Murthy, A. Didonna, B. Grin, E. Israeli, R. Perrot, P. Bomont, J.P. Julien, E. Kuczmarski, P. Opal, and R.D. Goldman. 2013. Giant axonal neuropathy-associated gigaxonin mutations impair intermediate filament protein degradation. *J Clin Invest*. 123:1964-1975.

Mavrakis, M., and M.A. Juanes. 2023. The compass to follow: Focal adhesion turnover. *Curr Opin Cell Biol*. 80:102152.

Meiring, J.C.M., I. Grigoriev, W. Nijenhuis, L.C. Kapitein, and A. Akhmanova. 2022. Opto-katanin, an optogenetic tool for localized, microtubule disassembly. *Curr Biol*. 32:4660-4674.

Mendez, M.G., S.I. Kojima, and R.D. Goldman. 2010. Vimentin induces changes in cell shape, motility, and adhesion during the epithelial to mesenchymal transition. *FASEB J*. 24:1838-1851.

Mendez, M.G., D. Restle, and P.A. Janmey. 2014. Vimentin enhances cell elastic behavior and protects against compressive stress. *Biophys J*. 107:314-323.

Messica, Y., A. Laser-Azogui, T. Volberg, Y. Elisha, K. Lysakovskaia, R. Eils, E. Gladilin, B. Geiger, and R. Beck. 2017. The role of Vimentin in Regulating Cell Invasive Migration in Dense Cultures of Breast Carcinoma Cells. *Nano Lett*. 17:6941-6948.

Mohan, R., and P. Bargagna-Mohan. 2016. The Use of Withaferin A to Study Intermediate Filaments. *Methods Enzymol*. 568:187-218.

Mohanasundaram, P., L.S. Coelho-Rato, M.K. Modi, M. Urbanska, F. Lautenschläger, F. Cheng, and J.E. Eriksson. 2022. Cytoskeletal vimentin regulates cell size and autophagy through mTORC1 signaling. *PLOS Biol*. 20:e3001737.

Nekrasova, O.E., M.G. Mendez, I.S. Chernoivanenko, P.A. Tyurin-Kuzmin, E.R. Kuczmarski, V.I. Gelfand, R.D. Goldman, and A.A. Minin. 2011. Vimentin intermediate filaments modulate the motility of mitochondria. *Mol Biol Cell*. 22:2282-2289.

Nijenhuis, W., M.M.P.v. Grinsven, and L.C. Kapitein. 2020. An optimized toolbox for the optogenetic control of intracellular transport. *J Cell Biol*. 219:e201907149.

Nishizawa, M., I. Izawa, A. Inoko, Y. Hayashi, K. Nagata, T. Yokoyama, J. Usukura, and M. Inagaki. 2005. Identification of trichoplein, a novel keratin filament-binding protein. *J Cell Sci*. 118:1081-1090.

Nixon-Abell, J., C.J. Obara, A.V. Weigel, D. Li, W.R. Legant, C.S. Xu, H.A. Pasolli, K. Harvey, H.F. Hess, E. Betzig, C. Blackstone, and J. Lippincott-Schwartz. 2016. Increased spatiotemporal resolution reveals highly dynamic dense tubular matrices in the peripheral ER. *Science*. 354:aaf3928.

Ostrowska-Podhorodecka, Z., I. Ding, M. Norouzi, and C.A. McCulloch. 2022. Impact of Vimentin on Regulation of Cell Signaling and Matrix Remodeling. *Front Cell Dev Biol*. 10:869069.

Özkan, N., M. Koppers, I. van Soest, A. van Harten, D. Jurriens, N. Liv, J. Klumperman, L.C. Kapitein, C.C. Hoogenraad, and G.G. Farías. 2021. ER – lysosome contacts at a pre-axonal region regulate axonal lysosome availability. *Nat Commun*. 12:4493.

Paulin, D., A. Lilienbaum, S. Kardjian, O. Agbulut, and Z. Li. 2022. Vimentin: Regulation and pathogenesis. *Biochimie*. 197:96-112.

Petitjean, II, Q.D. Tran, A. Goutou, Z. Kabir, G. Wiche, C. Leduc, and G.H. Koenderink. 2024. Reconstitution of cytolinker-mediated crosstalk between actin and vimentin. *Eur J Cell Biol*. 103:151403.

Pollock, R., R. Issner, K. Zoller, S. Natesan, V.M. Rivera, and T. Clackson. 2000. Delivery of a stringent dimerizer-regulated gene expression system in a single retroviral vector. *Proc Natl Acad Sci U S A*. 97:13221-13226.

Prahlad, V., M. Yoon, R.D. Moir, R.D. Vale, and R.D. Goldman. 1998. Rapid movements of vimentin on microtubule tracks: Kinesin-dependent assembly of intermediate filament networks. *J Cell Biol*. 143:159-170.

Reed, N.A., D. Cai, T.L. Blasius, G.T. Jih, E. Meyhofer, J. Gaertig, and K.J. Verhey. 2006. Microtubule acetylation promotes kinesin-1 binding and transport. *Curr Biol*. 16:2166-2172.

Ridge, K.M., J.E. Eriksson, M. Pekny, and R.D. Goldman. 2022. Roles of vimentin in health and disease. *Genes Dev*. 36:391-407.

Ridge, K.M., D. Shumaker, A. Robert, C. Hookway, V.I. Gelfand, P.A. Janmey, J. Lowery, M. Guo, D.A. Weitz, E. Kuczmarski, and R.D. Goldman. 2016. Methods for Determining the Cellular Functions of Vimentin Intermediate Filaments. *Methods Enzymol*. 568:389-426.

Robert, A., P. Tian, S.A. Adam, M. Kittisopikul, K. Jaqaman, R.D. Goldman, and V.I. Gelfand. 2019. Kinesin-dependent transport of keratin filaments: a unified mechanism for intermediate filament transport. *FASEB J*. 33:388-399.

Saldanha, R., M.T.H. Thanh, N. Krishnan, H. Hehnly, and A.E. Patteson. 2023. Vimentin supports cell polarization by enhancing centrosome function and microtubule acetylation. *bioRxiv*:2023.2002.2017.528977.

Schaedel, L., C. Lorenz, A.V. Schepers, S. Klumpp, and S. Köster. 2021. Vimentin intermediate filaments stabilize dynamic microtubules by direct interactions. *Nat Commun*. 12:3799.

Schwarz, N., R. Windoffer, T.M. Magin, and R.E. Leube. 2015. Dissection of keratin network formation, turnover and reorganization in living murine embryos. *Sci Rep*. 5:9007.

Sha, Y., D. Haensel, G. Gutierrez, H. Du, X. Dai, Q. Nie, Y. Sha, D. Haensel, G. Gutierrez, H. Du, X. Dai, and Q. Nie. 2019. Intermediate cell states in epithelial-to-mesenchymal transition. *Phys Biol*. 16:021001.

Shaebani, M.R., L. Stankevicins, D. Vesperini, M. Urbanska, D.A.D. Flormann, E. Terriac, A.K.B. Gad, F. Cheng, J.E. Eriksson, and F. Lautenschläger. 2022. Effects of vimentin on the migration, search efficiency, and mechanical resilience of dendritic cells. *Biophys J*. 121:3950-3961.

Smal, I., K. Draegestein, N. Galjart, W. Niessen, and E. Meijering. 2008. Particle filtering for multiple object tracking in dynamic fluorescence microscopy images: application to microtubule growth analysis. *IEEE Trans Med Imaging*. 27:789-804.

Strelkov, S.V., H. Herrmann, N. Geisler, T. Wedig, R. Zimbelmann, U. Aebi, and P. Burkhard. 2002. Conserved segments 1A and 2B of the intermediate filament dimer: their atomic structures and role in filament assembly. *EMBO J*. 21:1255-1266.

Swoger, M., S. Gupta, E.E. Charrier, M. Bates, H. Hehnly, and A.E. Patteson. 2022. Vimentin Intermediate Filaments Mediate Cell Morphology on Viscoelastic Substrates. *ACS Appl Bio Mater*. 5:552-561.

Trogden, K.P., R.A. Battaglia, P. Kabiraj, V.J. Madden, H. Herrmann, and N.T. Snider. 2018. An image-based small-molecule screen identifies vimentin as a pharmacologically relevant target of simvastatin in cancer cells. *FASEB J*. 32:2841-2854.

Usman, S., H. Aldehlawi, T.K.N. Nguyen, M.T. Teh, and A. Waseem. 2022. Impact of N-Terminal Tags on De Novo Vimentin Intermediate Filament Assembly. *Int J Mol Sci*. 23: 6349.

Wiche, G., and M.A. Baker. 1982. Cytoplasmic network arrays demonstrated by immunolocalization using antibodies to a high molecular weight protein present in cytoskeletal preparations from cultured cells. *Exp Cell Res*. 138:15-29.

Wiche, G., and L. Winter. 2011. Plectin isoforms as organizers of intermediate filament cytoarchitecture. *Bioarchitecture*. 1:14-20.

Zhu, W., A. Cowie, G.W. Wasfy, L.Z. Penn, B. Leber, and D.W. Andrews. 1996. Bcl-2 mutants with restricted subcellular location reveal spatially distinct pathways for apoptosis in different cell types. *EMBO J*. 15:4130-4141.

Figure 1

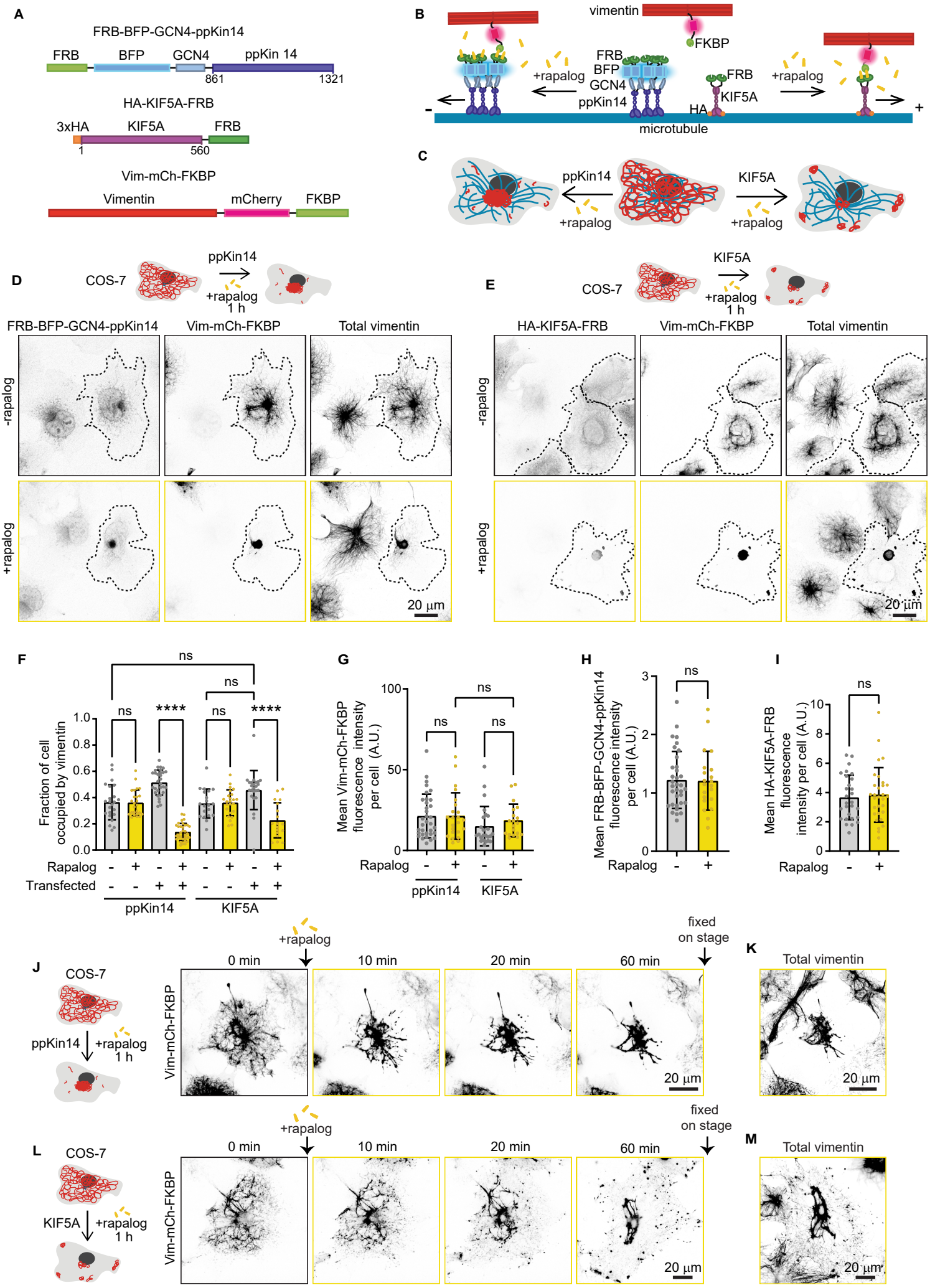
A
FRB-BFP-GCN4-ppKin14
FRB
BFP
GCN4
ppKin 14
861
1321
HA-KIF5A-FRB
3xHA
KIF5A
FRB
1
560
Vim-mCh-FKBP
Vimentin
mCherry
FKBP
B
vimentin
FKBP
FRB
BFP
GCN4
ppKin14
+rapalog
FRB
KIF5A
HA
+rapalog
-
+
microtubule
C
ppKin14
+rapalog
KIF5A
+rapalog
D
COS-7
ppKin14
+rapalog
1 h
FRB-BFP-GCN4-ppKin14
Vim-mCh-FKBP
Total vimentin
-rapalog
+rapalog
20 µm
E
COS-7
KIF5A
+rapalog
1 h
HA-KIF5A-FRB
Vim-mCh-FKBP
Total vimentin
-rapalog
+rapalog
20 µm
F
Fraction of cell occupied by vimentin
ns
ns
****
ns
ns
****
Rapalog
Transfected
ppKin14
KIF5A
G
Mean Vim-mCh-FKBP fluorescence intensity per cell (A.U.)
ns
ns
ns
Rapalog
ppKin14
KIF5A
H
Mean FRB-BFP-GCN4-ppKin14 fluorescence intensity per cell (A.U.)
ns
Rapalog
I
Mean HA-KIF5A-FRB fluorescence intensity per cell (A.U.)
ns
Rapalog
J
COS-7
ppKin14
+rapalog
1 h
+rapalog
fixed on stage
0 min
10 min
20 min
60 min
Vim-mCh-FKBP
20 µm
K
Total vimentin
20 µm
L
COS-7
KIF5A
+rapalog
1 h
+rapalog
fixed on stage
0 min
10 min
20 min
60 min
Vim-mCh-FKBP
20 µm
M
Total vimentin
20 µm

Figure 2

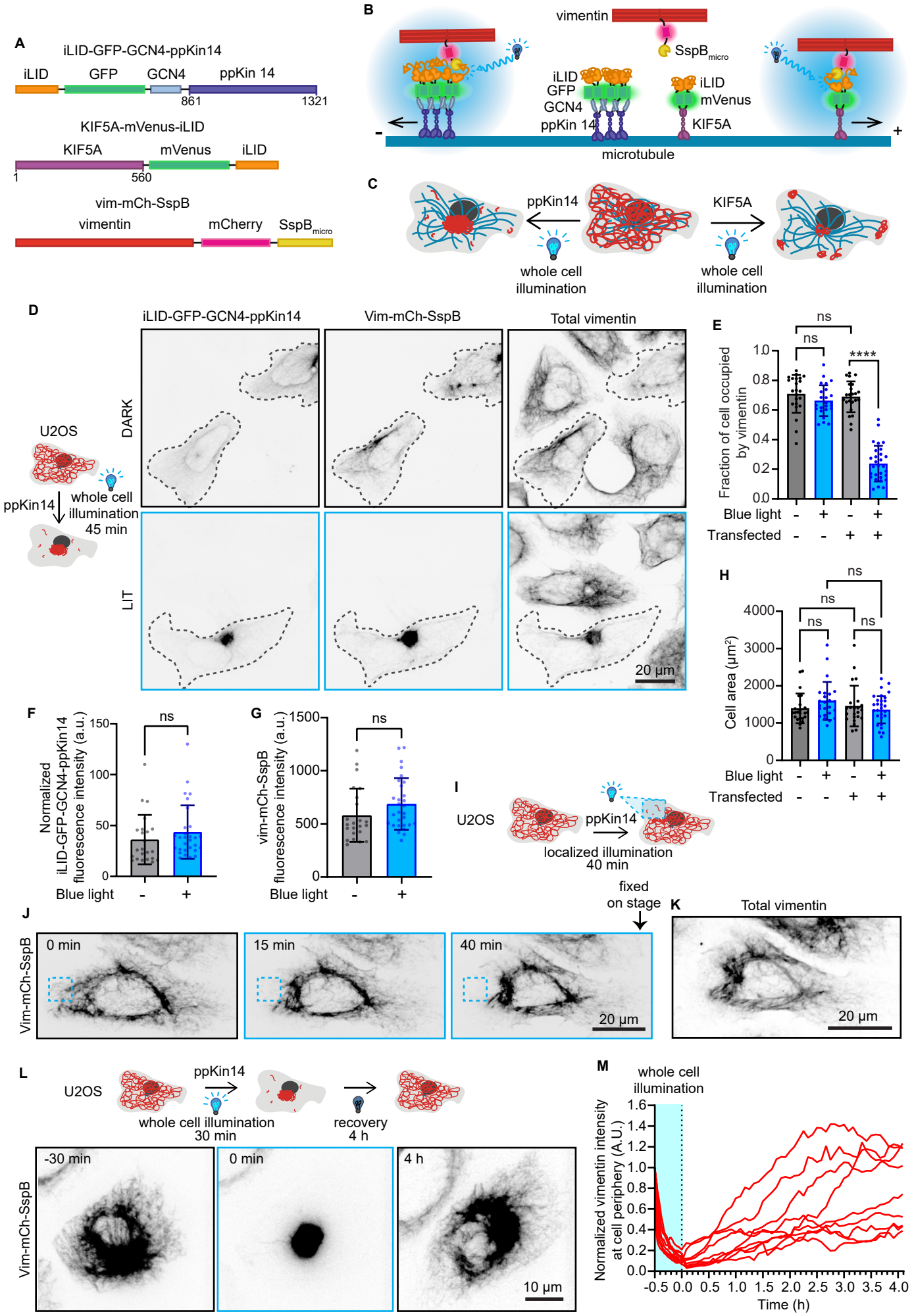
A
iLID-GFP-GCN4-ppKin14
iLID
GFP
GCN4
ppKin 14
861
1321
KIF5A-mVenus-iLID
KIF5A
mVenus
iLID
1
560
vim-mCh-SspB
vimentin
mCherry
SspB micro
B
vimentin
SspB micro
iLID
GFP
GCN4
ppKin 14
iLID
mVenus
KIF5A
microtubule
C
ppKin14
whole cell illumination
KIF5A
whole cell illumination
D
iLID-GFP-GCN4-ppKin14
Vim-mCh-SspB
Total vimentin
DARK
LIT
U2OS
ppKin14
whole cell illumination 45 min
20 µm
E
Fraction of cell occupied by vimentin
ns
ns
****
Blue light
Transfected
H
Cell area (µm²)
ns
ns
ns
ns
Blue light
Transfected
F
Normalized iLID-GFP-GCN4-ppKin14 fluorescence intensity (a.u.)
ns
Blue light
G
vim-mCh-SspB fluorescence intensity (a.u.)
ns
Blue light
I
U2OS
ppKin14
localized illumination 40 min
fixed on stage
J
Vim-mCh-SspB
0 min
15 min
40 min
20 µm
K
Total vimentin
20 µm
L
U2OS
ppKin14
whole cell illumination 30 min
recovery 4 h
Vim-mCh-SspB
-30 min
0 min
4 h
10 µm
M
whole cell illumination
Normalized vimentin intensity at cell periphery (A.U.)
Time (h)

Figure 3

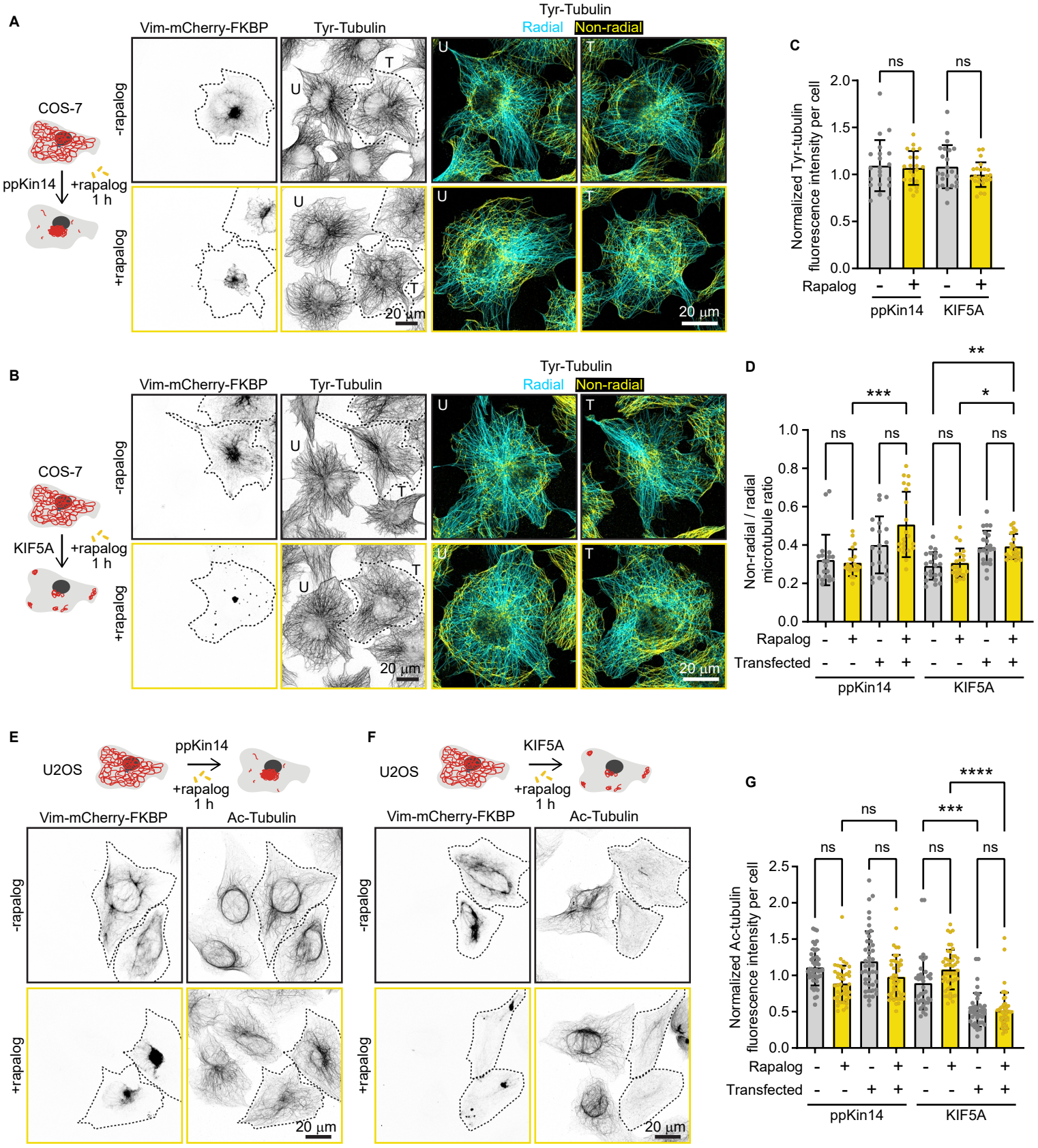
A
Vim-mCherry-FKBP
Tyr-Tubulin
Tyr-Tubulin
Radial
Non-radial
COS-7
ppKin14
+rapalog
1 h
-rapalog
+rapalog
U
T
20 µm
B
KIF5A
C
Normalized Tyr-tubulin fluorescence intensity per cell
ns
Rapalog
ppKin14
KIF5A
D
Non-radial / radial microtubule ratio
Transfected
E
U2OS
Ac-Tubulin
F
G
Normalized Ac-tubulin fluorescence intensity per cell
****
***
**
*

Figure 4

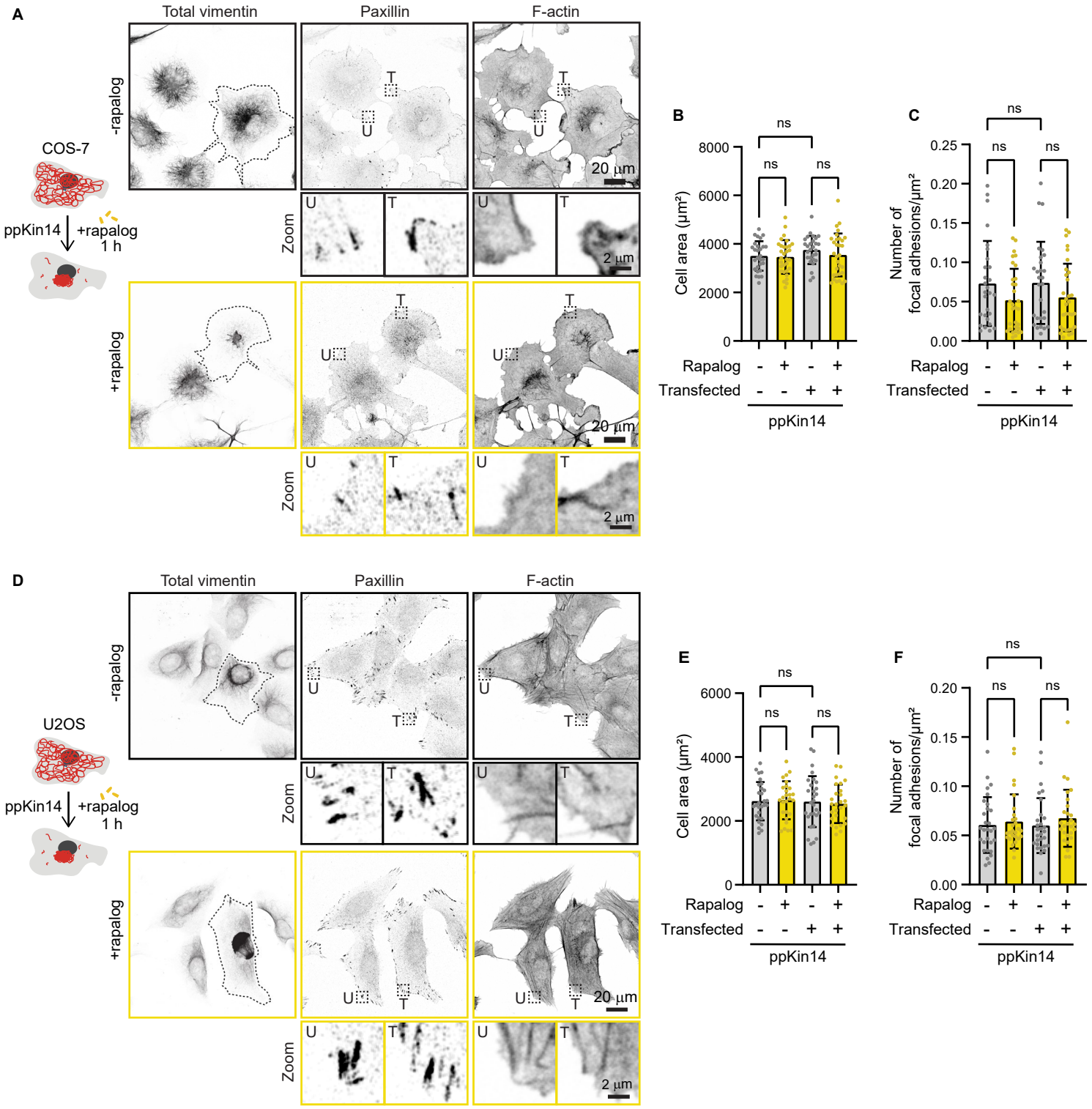
A
Total vimentin
Paxillin
F-actin
-rapalog
+rapalog
COS-7
ppKin14
+rapalog
1 h
Zoom
T
U
20 µm
2 µm
B
C
ns
Cell area (µm²)
Number of focal adhesions/µm²
Rapalog
Transfected
ppKin14
D
U2OS
E
F

Figure 5

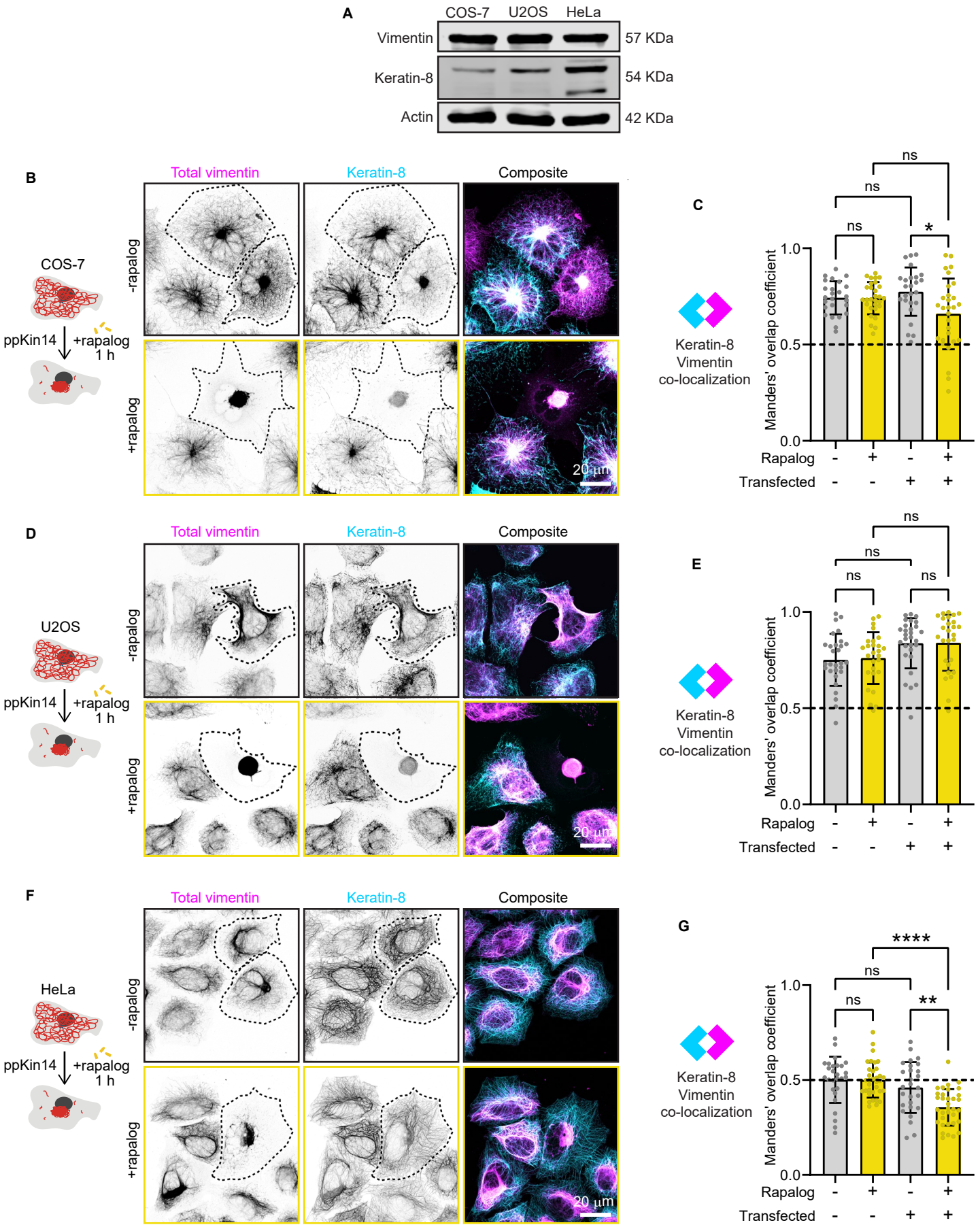
A
COS-7
U2OS
HeLa
Vimentin
Keratin-8
Actin
57 KDa
54 KDa
42 KDa
B
Total vimentin
Keratin-8
Composite
COS-7
ppKin14
+rapalog
1 h
-rapalog
+rapalog
20 µm
C
Keratin-8
Vimentin
co-localization
Manders' overlap coefficient
1.0
0.5
0.0
ns
ns
ns
*
Rapalog
Transfected
D
U2OS
E
ns
ns
ns
ns
F
HeLa
G
****
ns
ns
**

Figure 6

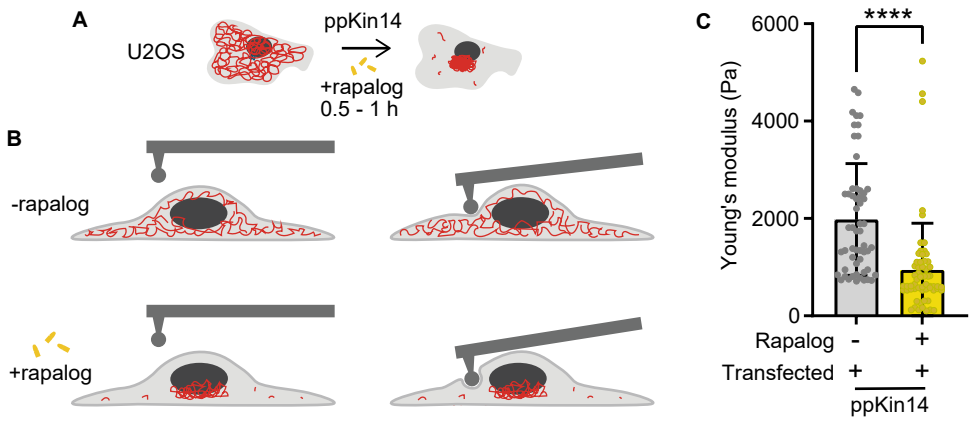
A
U2OS
ppKin14
+rapalog
0.5 - 1 h
B
-rapalog
+rapalog
C
****
Young's modulus (Pa)
6000
4000
2000
0
Rapalog - +
Transfected + +
ppKin14

Figure 7

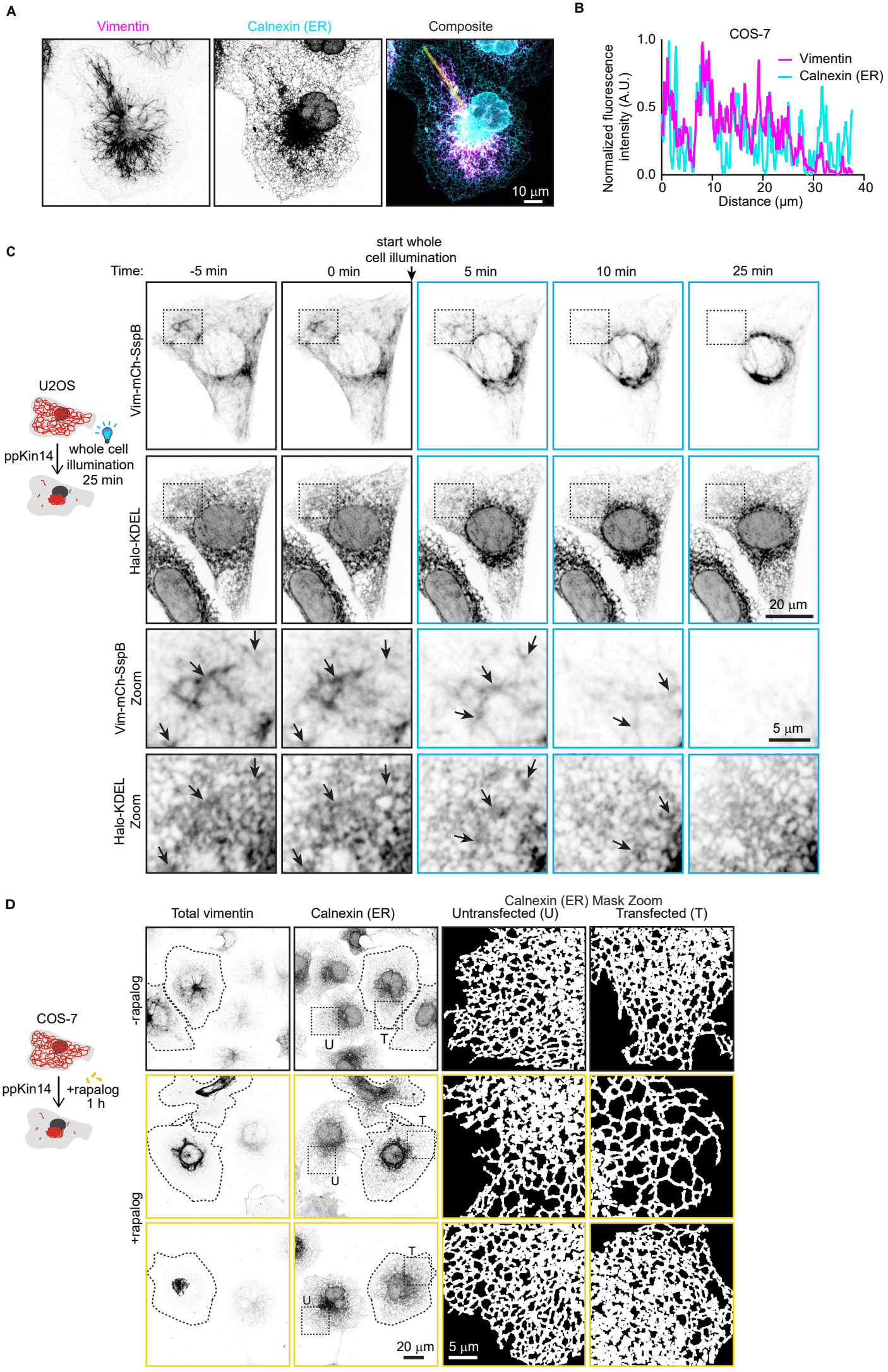
A
Vimentin
Calnexin (ER)
Composite
10 µm
B
COS-7
Vimentin
Calnexin (ER)
Normalized fluorescence intensity (A.U.)
1.0
0.5
0.0
0
10
20
30
40
Distance (µm)
C
start whole cell illumination
Time:
-5 min
0 min
5 min
10 min
25 min
U2OS
ppKin14
whole cell illumination 25 min
Vim-mCh-SspB
Halo-KDEL
Vim-mCh-SspB Zoom
Halo-KDEL Zoom
20 µm
5 µm
D
Total vimentin
Calnexin (ER)
Calnexin (ER) Mask Zoom
Untransfected (U)
Transfected (T)
COS-7
ppKin14
+rapalog 1 h
-rapalog
+rapalog
U
T
20 µm
5 µm

Figure 8

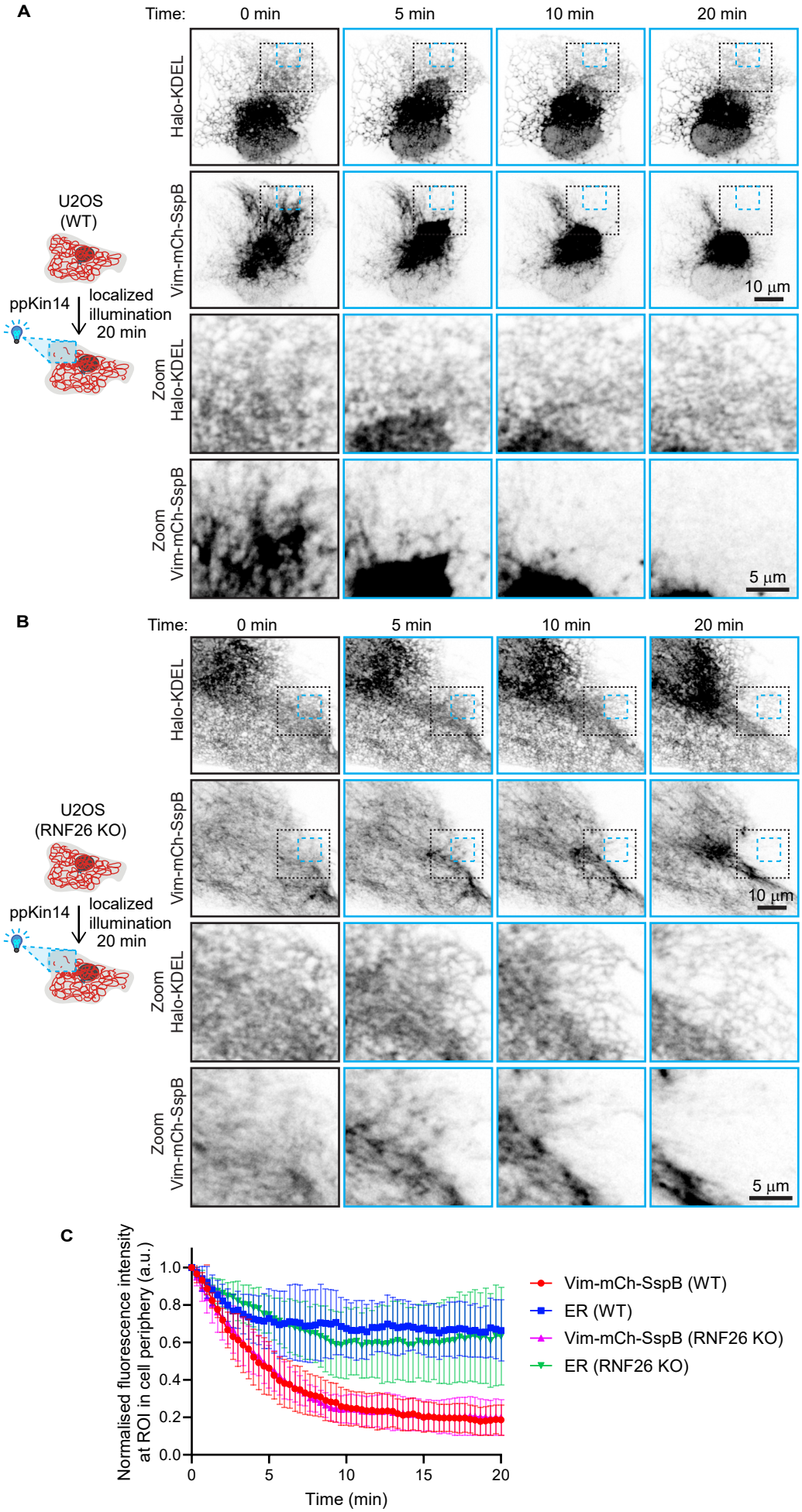
A
Time:
0 min
5 min
10 min
20 min
Halo-KDEL
Vim-mCh-SspB
Zoom Halo-KDEL
Zoom Vim-mCh-SspB
U2OS (WT)
ppKin14
localized illumination 20 min
10 µm
5 µm
B
U2OS (RNF26 KO)
C
Normalised fluorescence intensity at ROI in cell periphery (a.u.)
Time (min)
Vim-mCh-SspB (WT)
ER (WT)
Vim-mCh-SspB (RNF26 KO)
ER (RNF26 KO)

Figure 9

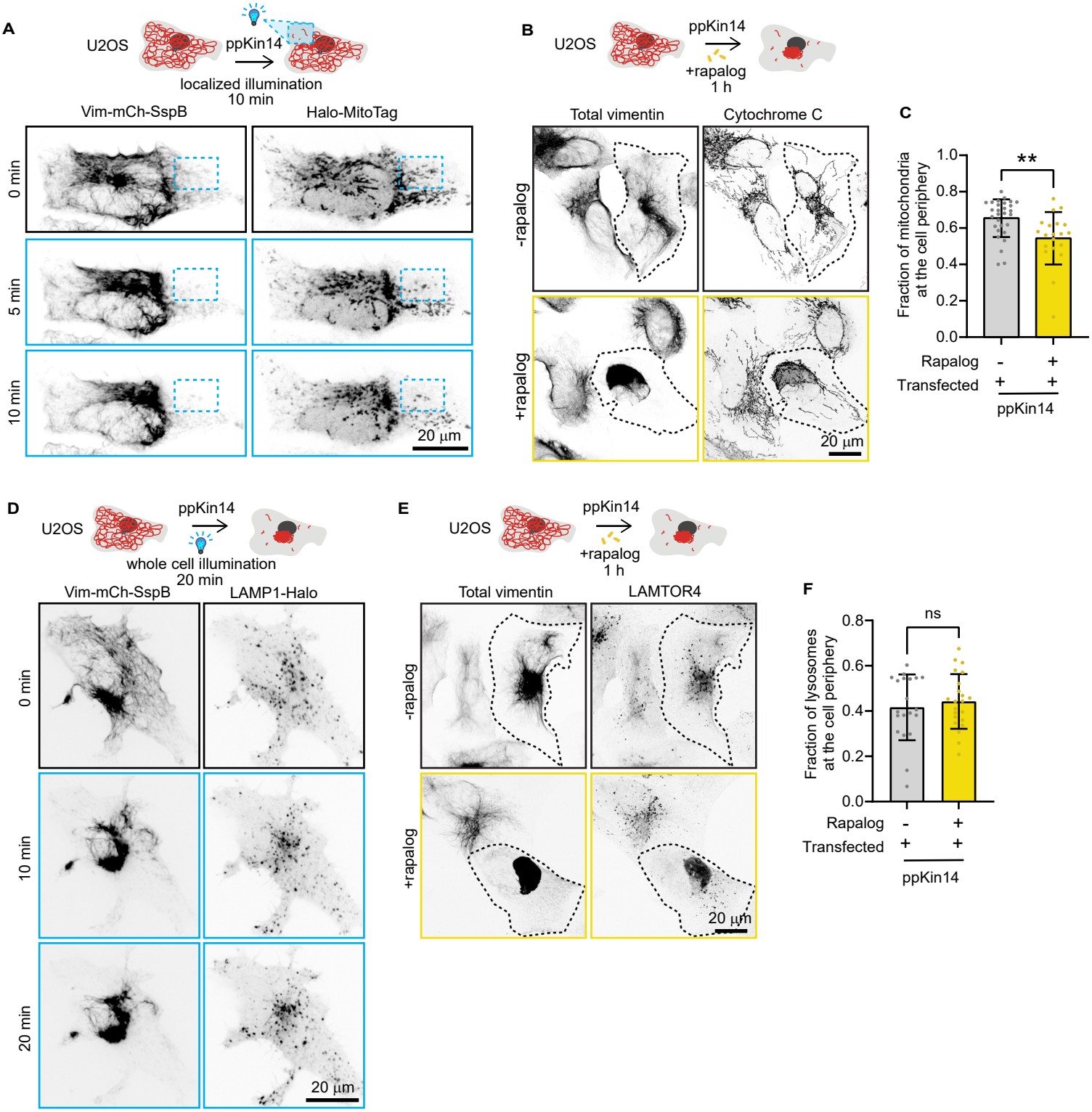
A
U2OS
ppKin14
localized illumination
10 min
Vim-mCh-SspB
Halo-MitoTag
0 min
5 min
10 min
20 µm
B
U2OS
ppKin14
+rapalog
1 h
Total vimentin
Cytochrome C
-rapalog
+rapalog
20 µm
C
Fraction of mitochondria at the cell periphery
1.0
0.8
0.6
0.4
0.2
0.0
**
Rapalog - +
Transfected + +
ppKin14
D
U2OS
ppKin14
whole cell illumination
20 min
Vim-mCh-SspB
LAMP1-Halo
0 min
10 min
20 min
20 µm
E
U2OS
ppKin14
+rapalog
1 h
Total vimentin
LAMTOR4
-rapalog
+rapalog
20 µm
F
Fraction of lysosomes at the cell periphery
0.8
0.6
0.4
0.2
0.0
ns
Rapalog - +
Transfected + +
ppKin14

Figure S1

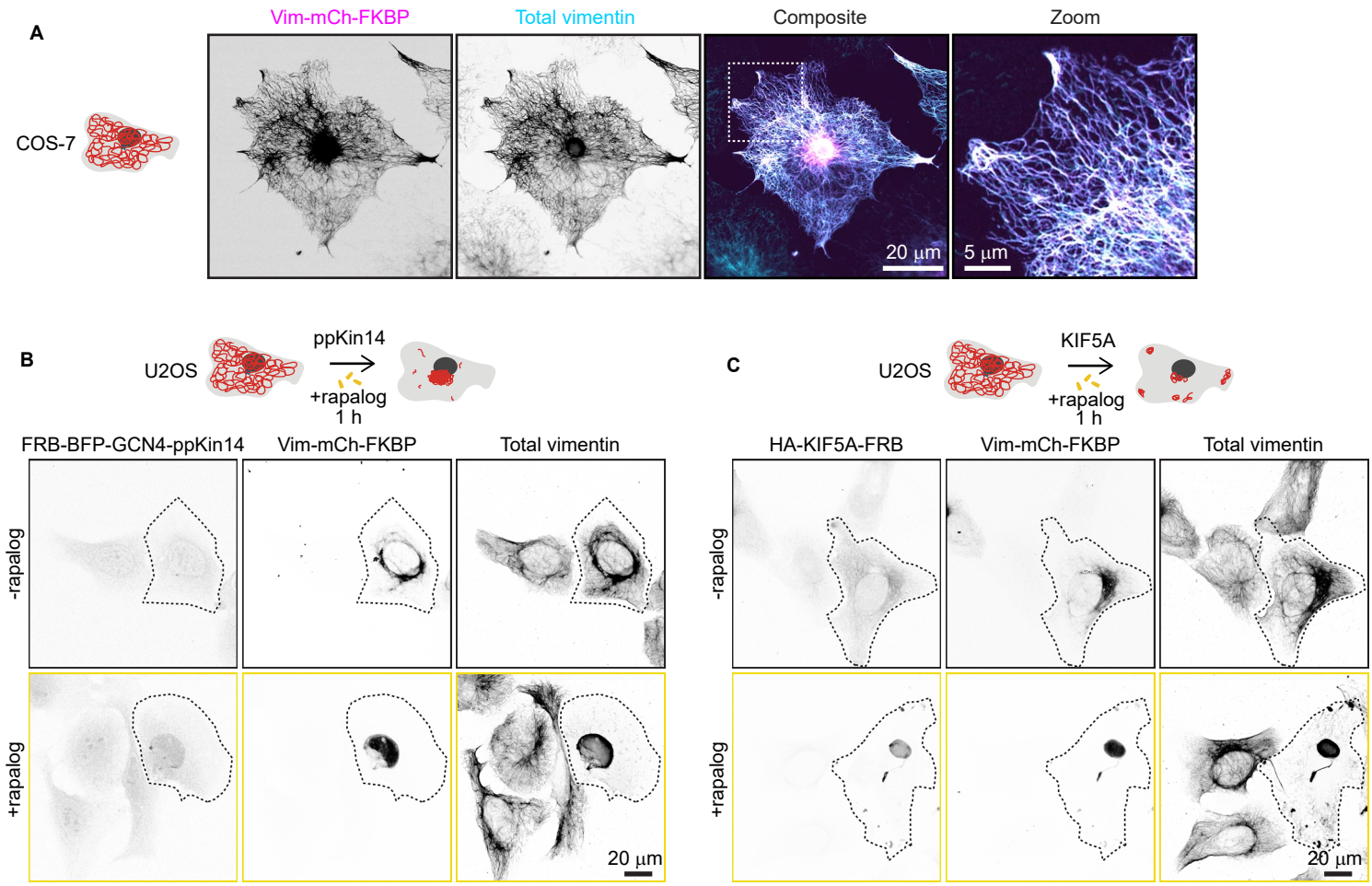
A
COS-7
Vim-mCh-FKBP
Total vimentin
Composite
Zoom
20 µm
5 µm
B
U2OS
ppKin14
+rapalog
1 h
FRB-BFP-GCN4-ppKin14
Vim-mCh-FKBP
Total vimentin
-rapalog
+rapalog
20 µm
C
U2OS
KIF5A
+rapalog
1 h
HA-KIF5A-FRB
Vim-mCh-FKBP
Total vimentin
-rapalog
+rapalog
20 µm

Figure S2

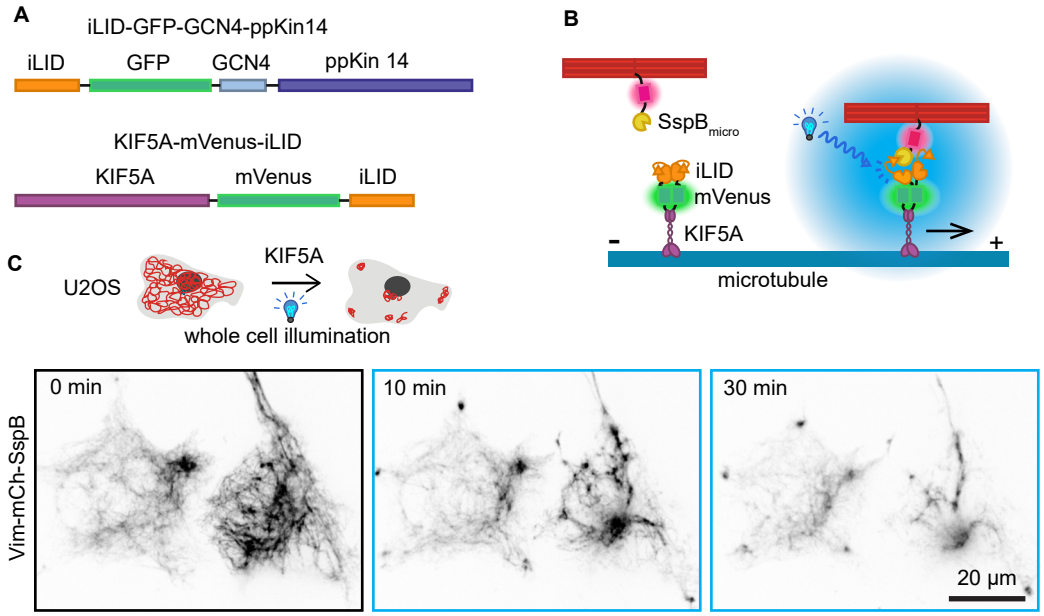
A
iLID-GFP-GCN4-ppKin14
iLID
GFP
GCN4
ppKin 14
KIF5A-mVenus-iLID
KIF5A
mVenus
iLID
B
SspB micro
iLID
mVenus
KIF5A
-
+
microtubule
C
U2OS
KIF5A
whole cell illumination
Vim-mCh-SspB
0 min
10 min
30 min
20 µm

Figure S3

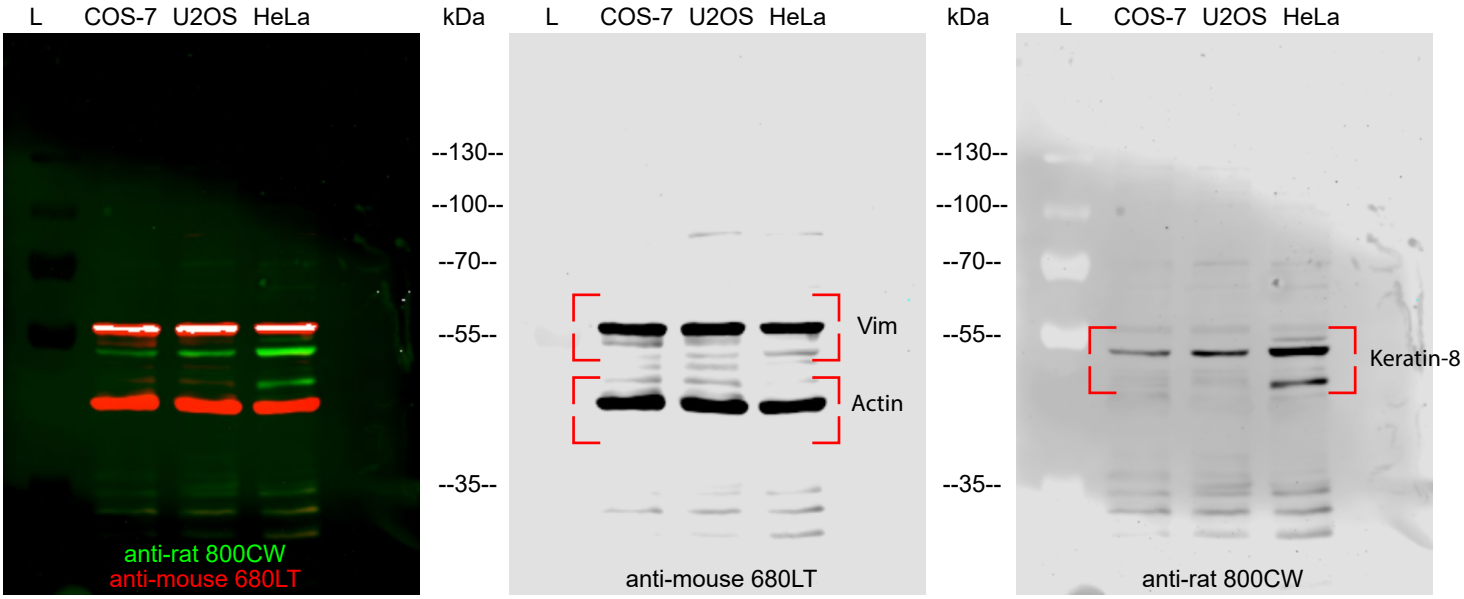
L
COS-7
U2OS
HeLa
kDa
--130--
--100--
--70--
--55--
--35--
anti-rat 800CW
anti-mouse 680LT
L
COS-7
U2OS
HeLa
Vim
Actin
anti-mouse 680LT
kDa
--130--
--100--
--70--
--55--
--35--
L
COS-7
U2OS
HeLa
Keratin-8
anti-rat 800CW

Figure S4

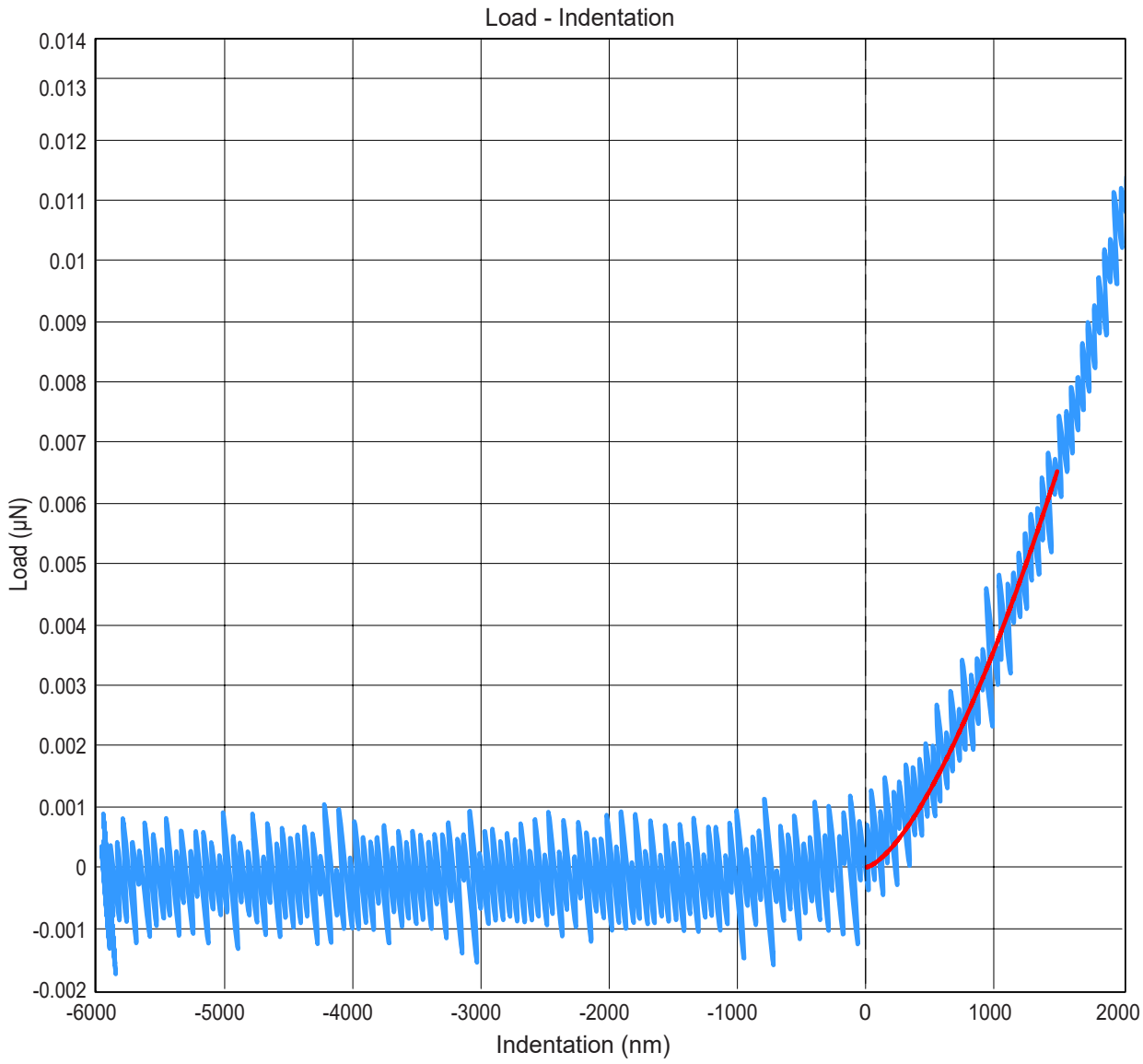
Load - Indentation
Load (µN)
0.014
0.013
0.012
0.011
0.01
0.009
0.008
0.007
0.006
0.005
0.004
0.003
0.002
0.001
0
-0.001
-0.002
-6000
-5000
-4000
-3000
-2000
-1000
0
1000
2000
Indentation (nm)